Monthly Notices of the ROYAL ASTRONOMICAL SOCIETY

MNRAS **545,** 1–25 (2026)
Advance Access publication 2025 October 7

https://doi.org/10.1093/mnras/staf1703

The mass of the exo-Venus Gliese 12 b, as revealed by HARPS-N, ESPRESSO, and CARMENES

Daisy A. Turner [1★] Yoshi Nike Emilia Eschen [2] Felipe Murgas,[3,4] Annelies Mortier [1] Thomas G. Wilson [2] Jorge Fernández Fernández,[2] Nicole Gromek,[5] Giuseppe Morello,[6,7] Hugo M. Tabernero,[8,9] Jo Ann Egger,[10] Shreyas Vissapragada,[11] José A. Caballero,[12] Stefan Dreizler,[13] Alix Violet Freckelton,[1] Artie P. Hatzes,[14] Ben Scott Lakeland,[1] Evangelos Nagel,[13] Luca Naponiello,[15] Siegfried Vanaverbeke,[16,17] Alexander Venner,[18] María Rosa Zapatero Osorio,[12] Pedro J. Amado,[6] Víctor J. S. Béjar,[3,4] Aldo Stefano Bonomo,[15] Lars A. Buchhave,[19] Andrew Collier Cameron,[20] Ilaria Carleo,[15] Priyanka Chaturvedi,[14,21] Ryan Cloutier,[5] Mario Damasso,[15] Mangesh Daspute,[22] Shishir Dholakia,[18] Sjoerd Dufoer,[16] Xavier Dumusque,[23] Aldo Fabricio Martinez Fiorenzano,[24] Adriano Ghedina,[24] Avet Harutyunyan,[24] Enrique Herrero,[9] Ancy Anna John,[1] Jorge Lillo-Box,[12] Nicolas Lodieu,[3,4] Mercedes López-Morales,[25] Luca Malavolta,[26,27] Luigi Mancini,[15,28,29] Giacomo Mantovan,[26,27] David Montes,[30] Juan Carlos Morales,[8,9] Belinda Nicholson,[18] Jaume Orell-Miquel,[31] Larissa Palethorpe,[32,33] Enric Palle,[3,4] Andreas Quirrenbach,[34] Sabine Reffert,[34] Ansgar Reiners,[13] Ignasi Ribas,[8,9] Ken Rice,[32,33] André M. Silva,[35,36] Alessandro Sozzetti,[15] Manu Stalport,[37,38] Lev Tal-Or,[22,39] Trifon Trifonov,[34,40] Stéphane Udry[23] and Mathias Zechmeister[13]

Affiliations are listed at the end of the paper

Accepted 2025 October 3. Received 2025 October 3; in original form 2025 June 25

ABSTRACT

Small temperate planets are prime targets for exoplanet studies due to their possible similarities with the rocky planets in the Solar system. M dwarfs are promising hosts since the planetary signals are within our current detection capabilities. Gliese 12 b is a Venus-sized temperate planet orbiting a quiet M dwarf. We present here the first precise mass measurement of this small exoplanet. We performed a detailed analysis using HARPS-N (High Accuracy Radial velocity Planet Searcher for the Northern Hemisphere), ESPRESSO (Echelle Spectrograph for Rocky Exoplanets and Stable Spectroscopic Observations), and CARMENES (Calar Alto high-Resolution search for M dwarfs with Exoearths with Near-infrared and optical Echelle Spectrographs) radial velocities, along with new and archival *TESS* (*Transiting Exoplanet Survey Satellite*), *CHEOPS* (*CHaracterising ExOPlanet Satellite*), and MuSCAT2/3 (Multicolor Simultaneous Camera for studying Atmospheres of Transiting exoplanets) photometry data. From fitting the available data, we find that the planet has a radius of $R_{\rm p} = 0.93 \pm 0.06\,{\rm R}_{\oplus}$ and a mass of $M_{\rm p} = 0.95^{+0.29}_{-0.30}\,{\rm M}_{\oplus}$ (a 3.2σ measurement of the semi-amplitude $K = 0.67 \pm 0.21\,{\rm m\,s^{-1}}$), and is on an orbit with a period of $12.761418^{+0.000060}_{-0.000055}$ d. A variety of techniques were utilized to attenuate stellar activity signals. Gliese 12 b has an equilibrium temperature of $T_{\rm eq} = 317 \pm 8$ K, assuming an albedo of zero, and a density consistent with that of Earth and Venus ($\rho_{\rm p} = 6.4 \pm 2.4\,{\rm g\,cm^{-3}}$). We find that Gliese 12 b has a predominantly rocky interior and simulations indicate that it is unlikely to have retained any of its primordial gaseous envelope. The bulk properties of Gliese 12 b place it in an extremely sparsely populated region of both mass–radius and density–$T_{\rm eq}$ parameter space, making it a prime target for follow-up observations, including Lyman-α studies.

Key words: techniques: radial velocities – planets and satellites: detection – planets and satellites: individual: Gliese 12 b – planets and satellites: interiors – planets and satellites: terrestrial planets – stars: individual: Gliese 12.

1 INTRODUCTION

One of the principal motivators in the field of exoplanetary science is the desire to find planets that are analogous to Earth or other small Solar system planets, in size, mass, composition, and potential habitability. M dwarfs have emerged as especially promising targets, as their relatively low masses and radii facilitate the detection of small planets. Their habitable zones also lie closer in, meaning potentially habitable planets are on more detectable orbits. While there could be drawbacks with habitability for planets hosted by M dwarfs [e.g. lower ultraviolet (UV) flux, tidal locking], the possibility of life is

★ E-mail: dat936@student.bham.ac.uk

not ruled out for these planets (see A. L. Shields, S. Ballard & J. A. Johnson 2016, for a review).

Significant progress has been made in identifying small planets, primarily through large surveys. Since the first light of pioneering telescopes such as *CoRoT* (COnvection, ROtation and planetary Transits; A. Baglin 2003) and *Kepler* (W. J. Borucki et al. 2010), the detection of exoplanets has undergone a revolution, resulting in a dramatic increase in the rate of discoveries. These missions have demonstrated that small planets (here loosely defined as any planet with a radius smaller than $2\,R_\oplus$) are abundant, particularly around M dwarfs (e.g. C. D. Dressing & D. Charbonneau 2015; S. Sabotta et al. 2021).

As of 2025 May, around 6000 exoplanets had been detected[1] (J. L. Christiansen et al. 2025), with thousands of other targets identified as exoplanetary candidates, evidencing the vital part that space-based surveys play in establishing a selection of targets for follow-up. However, while these missions have revealed many small planets, the understanding of this population is incomplete without measurements of their masses.

Obtaining precise planetary mass measurements remains challenging and time consuming. This is especially true for planets with radial velocity (RV) semi-amplitudes of less than $1\,m\,s^{-1}$ (e.g. F. Pepe et al. 2011; T. G. Wilson et al. 2022; M. Stalport et al. 2025), a regime characteristic of Earth-mass planets around M dwarfs (e.g. O. D. S. Demangeon et al. 2021; A. S. Bonomo et al. 2023; F. Murgas et al. 2023; R. Basant et al. 2025). Such signals are further obscured by stellar activity, a considerable source of noise that is typically pronounced for faint M dwarfs such as Gliese 12. To achieve the precision necessary to characterize Earth-mass planets, data from high-resolution spectrographs, such as HARPS-N (High Accuracy Radial velocity Planet Searcher for the Northern Hemisphere; R. Cosentino et al. 2012), ESPRESSO (Echelle Spectrograph for Rocky Exoplanets and Stable Spectroscopic Observations; F. Pepe et al. 2014, 2021), and CARMENES (Calar Alto high-Resolution search for M dwarfs with Exoearths with Near-infrared and optical Echelle Spectrographs; A. Quirrenbach et al. 2014, 2018), are required.

Currently, very few Earth-sized planets have both precise mass and radius measurements. This small sample of planets acts as a critical benchmark to understand planet composition, formation, evolution, and habitability. With measurements of both radius and mass, the bulk density of a planet can be calculated, allowing for an understanding of its approximate interior structure and composition. We can furthermore use the mass and radius to simulate scenarios for the atmospheric evolution of a planet and infer its prospects for atmospheric characterization with, e.g. *James Webb Space Telescope* (*JWST*) or *Hubble Space Telescope* (*HST*). Accurate atmospheric parameters can only be obtained if the mass of the planet is known to a sufficient precision. With no measurement of a planet's mass, only tenuous approximations can be made, as the solutions for the envelope composition are degenerate (N. E. Batalha et al. 2019). Therefore, with more planetary information available, a planet's similarity to Solar system planets can more easily be gauged.

The transit of Gliese 12 b was discovered by *TESS* (*Transiting Exoplanet Survey Satellite*, TOI-6251), and using separate validation data, S. Dholakia et al. (2024) and M. Kuzuhara et al. (2024) announced the validation of this planet. Gliese 12 b is a planet with a radius close to $1\,R_\oplus$, putting it firmly in the Earth-like regime. It orbits its host star every $\sim$12.76 d. Since Gliese 12 is an M dwarf, this makes Gliese 12 b a temperate planet just outside the habitable zone as defined by R. K. Kopparapu et al. (2014).

While S. Dholakia et al. (2024) and M. Kuzuhara et al. (2024) did use RV measurements to validate the planet, its mass remained unmeasured due to an insufficient amount of data. This lack of data left key aspects unconstrained, such as its density, composition, and potential for life. In this study, we present the first mass measurement of Gliese 12 b using extremely precise RVs from three spectrographs: HARPS-N, ESPRESSO, and CARMENES.

In Section 2, we describe the data sets used in this work. This includes both photometry and spectroscopy. The host star and its properties are described in Section 3. We performed an individual photometry fit, an RV fit informed by the photometry fit, and a joint fit, all of which are described in Sections 4, 5, and 6, respectively. Finally, we discuss the implications of this new mass measurement in Section 7 and conclude in Section 8.

2 DATA

2.1 Photometry

Gliese 12 has been observed extensively, as described by S. Dholakia et al. (2024) and M. Kuzuhara et al. (2024). In this work, we use transit data from *TESS*, *CHEOPS* (*CHaracterising ExOPlanet Satellite*), MuSCAT2 (Multicolor Simultaneous Camera for studying Atmospheres of Transiting exoplanets), MuSCAT3, and long-term photometry from ASAS-SN (All-Sky Automated Survey for Supernovae), LCOGT (Las Cumbres Observatory Global Telescope), TJO (Telescopi Joan Oró), and E-EYE (Entre Encinas y Estrellas).

2.1.1 TESS

The *TESS* (G. R. Ricker et al. 2015; G. Ricker 2021) has observed Gliese 12 in a total of five sectors, each being approximately 27 d long. Four of these sectors were previously presented by S. Dholakia et al. (2024) and M. Kuzuhara et al. (2024), totalling around 135 d of coverage. The orbital period of Gliese 12 b was initially ambiguous, as the first few sectors of *TESS* data were consistent with periods of 12.76 or 25.52 d. Ultimately, in sectors 42, 43, 57, and 70, a total of five transits were identified, leading to the confirmation of a planetary orbital period of $\sim$12.76 d.

Gliese 12 was observed again in *TESS* sector 84, the first sector of Cycle 7, between 2024 October 01 and 26 (BJD 2460584.50–BJD 2460609.50). These data were released after the publication of S. Dholakia et al. (2024) and M. Kuzuhara et al. (2024), and two additional transits events were captured. These data were taken using CCD 3 on camera 1. In all, the data span approximately 105 d. We used the PDCSAP (Pre-search Data Conditioning Simple Aperture Photometry) data, downloaded from the MAST portal.[2]

2.1.2 CHEOPS

The *CHEOPS* (W. Benz et al. 2021) is a follow-up mission launched in 2019 with the goal to derive radii of planets more precisely. S. Dholakia et al. (2024) presented five *CHEOPS* visits of the transits of Gliese 12 b that were obtained in the *CHEOPS* AO-4 guest observers programmes with the IDs; ID:07 (PI: Palethorpe) and ID:12 (PI: Venner). Since then an additional visit has been obtained within the

[1] https://exoplanetarchive.ipac.caltech.edu

[2] https://mast.stsci.edu/

Table 1. Summary of the *CHEOPS* observations of Gliese 12 and the used detrending vectors.

Visit	Start date (UTC)	Duration (h)	Data points (no.)	File key	Efficiency (per cent)	Exp time (s)	Detrending vectors
1	2023-09-24T00:03:43	11.41	513	CH_PR240007_TG000101	74.9	60	t, x, y^2
2	2023-10-06T18:19:43	12.76	481	CH_PR240007_TG000102	62.8	60	–
3	2023-10-19T16:32:43	6.80	222	CH_PR240012_TG000701	54.3	60	–
4	2023-11-14T06:29:42	6.92	241	CH_PR240012_TG000702	57.9	60	–
5	2023-11-26T21:38:42	7.44	248	CH_PR240012_TG000101	55.5	60	x, t, $\cos(2\phi)$
6	2024-08-20T23:26:43	6.47	279	CH_PR240012_TG000801	71.7	60	smear, contam

ID:12 programme and a transit observed. The six available *CHEOPS* visits are summarized in Table 1.

As Gliese 12 is a rather faint target to be observed by *CHEOPS*, we re-extracted the photometry using the PSF Imagette Photometric Extraction (PIPE; A. Brandeker, J. A. Patel & B. M. Morris 2024) instead of the aperture photometry produced by *CHEOPS*' Data Reduction Pipeline (DRP; S. Hoyer et al. 2020). We analysed each visit individually using PYCHEOPS (P. F. L. Maxted et al. 2022) and JULIET (N. Espinoza, D. Kossakowski & R. Brahm 2019), a planet modelling tool using nested sampling and implementing BATMAN (L. Kreidberg 2015) to model the transits. We obtained the detrending vectors for each *CHEOPS* visit in PYCHEOPS via Bayes factor assessments of simultaneously fitting subsets of the detrending vectors with a transit model. We subsequently detrended the visits against the instrumental vectors using linear regressors in JULIET to accurately probe the detrending parameter space with the nested sampling algorithm provided in JULIET. The detrended vectors for each visit are reported in Table 1. We also applied a 3σ-clipping to the data, removing outliers that were more than 3σ away from the mean of the data. As the transit is shallow, no in-transit points were removed by this sigma clipping.

We note that there are an additional four opportunistic *CHEOPS* visits available from 2020 September 22 to 2021 September 19. However, since these do not cover any transits, we did not include these in any further analysis.

2.1.3 *MuSCAT*

As presented by M. Kuzuhara et al. (2024), two transits of Gliese 12 b have been observed with MuSCAT2 (N. Narita et al. 2019) and two transits with MuSCAT3 (N. Narita et al. 2020). Directly following the method of M. Kuzuhara et al. (2024), we detrended the data using a Gaussian process (GP) regression with a Matérn 3/2 kernel. Similar to our approach with the *CHEOPS* data, we performed this detrending for each visit separately.

2.1.4 *ASAS-SN*

We retrieved all available data from the ASAS-SN (B. J. Shappee et al. 2014; C. S. Kochanek et al. 2017). Photometry was recomputed via the ASAS-SN web portal, accounting for the proper motion of the star. After excluding poor-quality measurements, the data set contains 1019 V-band observations spanning 2012 January 20 to 2018 November 29 and 3678 g'-band measurements spanning 2017 September 21 to 2025 August 26. Outliers were removed using a 5-median absolute deviation clipping.

2.1.5 *LCOGT*

We obtained photometric observations with the LCOGT (T. M. Brown et al. 2013). The target star was observed using the 0.4 and 1.0 m telescopes in the V and B bands, respectively. For the B-band observations, we used an exposure time of 30 s and collected a total of 570 images between 2023 December 14 and 2025 January 16. For the V band, the exposure time was 300 s, and we collected 241 images between 2024 August 24 and 2024 December 26. The images were calibrated using the standard LCOGT BANZAI pipeline (C. McCully et al. 2018), and differential photometry was extracted with ASTROIMAGEJ (K. A. Collins et al. 2017).

Table 2. Summary of the RV observations.

Instrument	Number of RVs	Average error ($m\,s^{-1}$)	Standard deviation ($m\,s^{-1}$)
HARPS-N	76 (74)	1.43 (1.43)	2.88 (2.90)
ESPRESSO	35 (34)	0.35 (0.35)	1.90 (1.92)
CARMENES	93 (91)	1.77 (1.77)	3.38 (2.47)

Note. Values enclosed in brackets are calculated from data after outliers are excluded. For HARPS-N and ESPRESSO, the `S-BART` values were used.

2.1.6 *TJO*

A long-term photometric campaign of Gliese 12 was carried out using the 0.8 m TJO (J. Colomé et al. 2010) at the Montsec Observatory in Lleida, Spain. We obtained a total of 1106 R-band images between 2023 May 23 and 2025 January 09. The raw science images were calibrated using the ICAT pipeline (J. Colome & I. Ribas 2006).

2.1.7 *E-EYE*

We collected data with e-EYE,[3] a 16-inch Optimised Dall–Kirkhams reflector located at Fregenal de la Sierra in Badajoz, Spain. A total of 351 images were obtained: 175 in the V band and 176 in the R band. The observations span the period from 2023 December 14 to 2025 February 25. Image reduction and differential aperture photometry of the target and several reference stars were performed using the LESVEPHOTOMETRY package.[4]

2.2 Spectroscopy

In this work, we used three different spectroscopic data sets, taken by HARPS-N, ESPRESSO, and CARMENES. There is also the publicly available data from IRD used by M. Kuzuhara et al. (2024). We decided not to use the latter due to the difference in scatter as compared to the more stabilized data used in this work. Outliers within each used data set were removed (post-re-extraction in the case of HARPS-N and ESPRESSO) via identifying data points with uncertainties more than 3σ from the median uncertainty on an instrument-by-instrument basis. Summary statistics on the RVs

[3] https://www.e-eye.es/
[4] http://www.dppobservatory.net/

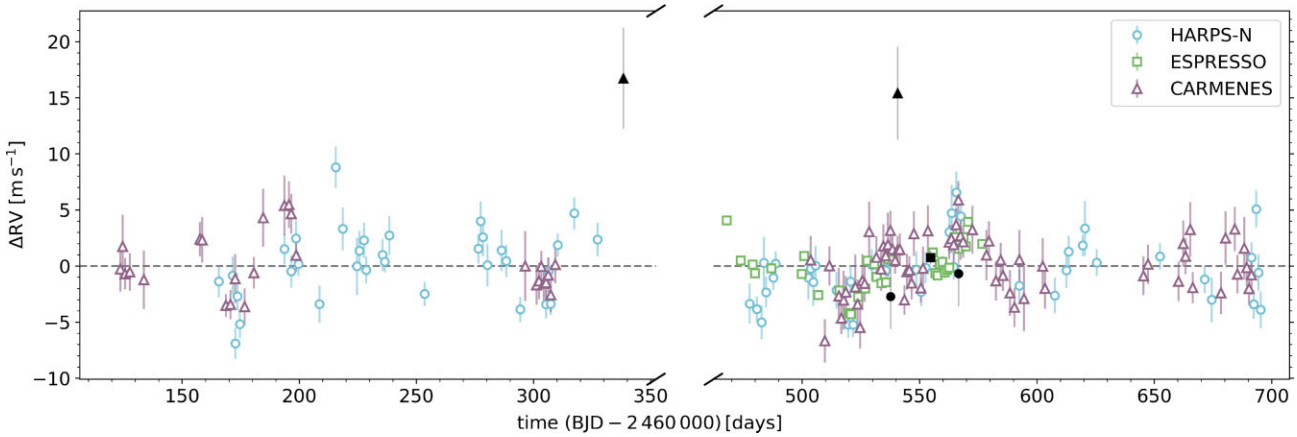

Figure 1. Gliese 12 RVs with offsets removed; HARPS-N, ESPRESSO, and CARMENES data are plotted as blue circles, green squares, and purple triangles, respectively. Uncertainties on the ESPRESSO RVs are smaller than the marker points. Outliers are indicated by the black, solid markers.

are mentioned in Table 2, and the full set of RVs used in our analyses are shown in Fig. 1.

2.2.1 *HARPS-N*

We obtained 87 observations with the HARPS-N spectrograph (R. Cosentino et al. 2012), a small subset of which was already published by S. Dholakia et al. (2024). HARPS-N is a high-precision, high-resolution echelle spectrograph installed on the Telescopio Nazionale Galileo (TNG) in La Palma, Spain. The instrument covers a wavelength range of 383–693 nm and has an average resolving power of $\mathcal{R} = 115\,000$. Observations were taken over four semesters, from 2023 August 09 to 2025 January 28 (BJD 2460165.66–BJD 2460704.35), spanning just under a year and a half. Thirteen observations were obtained via the Guaranteed Time Observation programme, with the remaining 63 data points collected as part of the HARPS-N Collaboration under programme A48TAC_59 (PI: L. Malavolta).

The target was observed with the second fibre pointed at the sky, with observations having an average exposure time of 1800 s. The data were processed with the standard HARPS-N DRS (Data Reduction Software version 3.0.1–X. Dumusque et al. 2021), with an M5 V mask used to obtain the cross-correlation functions (CCFs). Additionally, the DRS calculated several spectral activity indicators, including the S-index and Hα metric from the spectra. The median signal-to-noise ratio (S/N) in order 50 is 24.

To ensure homogeneity across all instruments, and accounting for the specific CCF shape of M dwarfs, activity indicators were re-extracted from the CCFs following M. Lafarga et al. (2020). An inverted Gaussian was fit to the CCF, from which the contrast, full width at half maximum (FWHM), and bisector inverse slope (BIS) were calculated. To obtain the BIS values, we followed the method outlined by D. Queloz et al. (2001), where the top and bottom regions of the CCF are defined as the sections between 60 and 90 per cent, and 10 and 40 per cent, respectively.

As Gliese 12 is an M dwarf, obtaining RVs using the CCF method is challenging due to the large number of spectral lines and their blending. Hence, we re-extracted the RVs using the Semi-Bayesian Approach for RVs with Template-matching[5] (`S-BART`; A. M. Silva et al. 2022), which is shown to be especially successful in its application to M dwarfs. Within this process, we re-extracted RVs for different quality checks including all combinations of RV steps (0.1, 0.5, and 1.0 m s^{-1}), RV limits (200, 500, and 1000 m s^{-1}), minimum order S/N (1.5, 5, and 10), airmasses (1.5, 2.0, 2.2, and 2.6), and RV errors (5, 6, 7, and 10 m s^{-1}), as well as the classical and Laplacian method `S-BART` applies (see A. M. Silva et al. 2022, for more detail). We selected the re-extracted RVs producing the lowest median error in `S-BART`. These are for an RV step of 0.1 m s^{-1}, RV limit of 500 m s^{-1}, minimum order S/N of 1.5, airmass of 1.5, RV errors of 5 m s^{-1}, and by using the Laplacian method. We note that the classical method provided very similar results but with slightly higher errors. This removed 11 data points whose spectra did not fulfil `S-BART`'s quality checks and left 76 HARPS-N RVs. The median error of the RVs in `S-BART` was reduced to 1.43 m s^{-1} as compared to 2.98 m s^{-1} from the DRS. The standard deviation of the RVs became 2.88 m s^{-1} from `S-BART` compared to 5.10 m s^{-1} from the DRS.

2.2.2 *ESPRESSO*

Gliese 12 was observed with ESPRESSO (F. Pepe et al. 2014, 2021), a high-resolution echelle spectrograph installed at the incoherent combined coudé facility of the Very Large Telescope at the Paranal Observatory, Chile. ESPRESSO is ultrastable, covers a wavelength range of 380–788 nm, and has an average resolving power of $\mathcal{R} =$ 140 000. A total of 35 observations were taken between 2024 June 06 to 2024 September 23 (BJD 2460467.90–BJD 2460576.75) as part of a Cycle P113 programme with ID:113.26RH (PI: Wilson). With an exposure time of 1200 s, we obtained a median S/N at ∼550 nm of 29.50. The data were processed through the standard ESPRESSO DRS (version 3.3.1) with an M5 V mask. Similar to the HARPS-N data, this produced CCFs as well as spectral activity indicators.

We again reprocessed the RVs using `S-BART` for all the combinations of quality checks stated above. We also selected the quality check combination producing RVs with the lowest median error of 0.35 m s^{-1} compared to a median error of 0.70 m s^{-1} from the DRS. This resulted in a standard deviation of 1.90 m s^{-1} for `S-BART` and 2.14 m s^{-1} for the DRS. For ESPRESSO, this is the case for an RV step of 0.1 m s^{-1}, RV limit of 200 m s^{-1}, minimum order S/N of 1.5, airmass of 1.5, and RV error of 7 m s^{-1}, as well as applying the Laplacian method in `S-BART`.

[5] https://github.com/iastro-pt/sBART

This method kept in all 35 RV observations taken by ESPRESSO. The RVs utilized in our analyses were those extracted using `S-BART`.

2.2.3 *CARMENES*

Gliese 12 was observed with the CARMENES spectrograph installed at the 3.5 m telescope of Calar Alto Observatory in Almería, Spain. CARMENES has two channels, one operating at visible wavelengths (VIS, spectral range 0.52–0.96 μm) and one operating at near-infrared wavelengths (NIR, spectral range 0.96–1.71 μm). The average spectral resolution of the VIS channel is $\mathcal{R} = 94\,600$ and the resolution of the NIR channel is $\mathcal{R} = 80\,400$ (A. Quirrenbach et al. 2014, 2018).

A total of 93 RV measurements were collected from 2023 June 28 to 2025 January 15 (BJD 2460123.59–BJD 2460691.34), and part of the data collected in 2023 was presented by M. Kuzuhara et al. (2024). The spectra were acquired with an exposure time of 1800 s. Data reduction was performed using the CARACAL pipeline (J. A. Caballero et al. 2016), which applies standard corrections for bias, flat field, and cosmic rays, and extracts spectra using the FOX optimal extraction algorithm (M. Zechmeister, G. Anglada-Escudé & A. Reiners 2014). Wavelength calibration was carried out following the procedure described by F. F. Bauer, M. Zechmeister & A. Reiners (2015). RV measurements were obtained with the template-matching algorithm SERVAL[6] (M. Zechmeister et al. 2018). The RV measurements were corrected for other effects such as barycentric motion, secular acceleration, instrumental drifts, and nightly zero-points (e.g. L. Tal-Or et al. 2018; T. Trifonov et al. 2018).

The 93 spectra have a median S/N of 90 measured at the spectral order centred at 746 nm (minimum S/N = 27 and maximum S/N = 118) in the VIS channel. The median value of the RV uncertainties are 1.76 m s^{-1} for the VIS channel, and 6.24 m s^{-1} for the NIR channel. In this work, we used only the VIS channel RVs, as they present significantly lower scatter than the NIR velocities.

3 HOST STAR CHARACTERIZATION

Gliese 12 is a nearby M dwarf with subsolar metallicity, likely belonging to the Galactic thin disc; see M. Cortés-Contreras et al. (2024) and S. Dholakia et al. (2024) for a discussion of the kinematics.

3.1 Stellar parameters

It was previously characterized by S. Dholakia et al. (2024) and M. Kuzuhara et al. (2024). Using the CARMENES data, we determined the stellar atmospheric parameters, namely $T_{\rm eff}$, log g, and [Fe/H], on the CARMENES template spectrum corrected for telluric absorption (E. Nagel et al. 2023) with the code STEPARSYN[7] (H. M. Tabernero et al. 2022) using the line list and model grid described by E. Marfil et al. (2021). We set the total line broadening to account for both the macroturbulence and the projected rotational velocity of the star ($v_{\rm broad}$, see H. M. Tabernero et al. 2022) to 2 km s^{-1}. This is supported by a model-independent determination using the projected rotational velocity ($v \sin i$) of A. Reiners et al. (2018). The luminosity was derived from the integration of the spectral energy distribution following C. Cifuentes et al. (2020) with updated photometry from *B* to *W*4 and *Gaia* DR3 parallax (Gaia Collaboration 2023). The stellar radius follows the Stefan–Boltzmann law and the stellar mass from the linear mass–radius relation given by A. Schweitzer et al. (2019). Table 3 summarizes our derived parameters based on the CARMENES data, which are easily consistent with the errors of the two previous characterizations.

Table 3. Gliese 12 stellar parameters used in this work.

Parameter	Unit	Value	Source
$T_{\rm eff}$	(K)	3328 ± 78	(a)
$M_\star$	($M_\odot$)	0.255 ± 0.013	(a)
$R_\star$	($R_\odot$)	0.265 ± 0.012	(a)
$\rho_\star$	(g cm^{-3})	$19.3^{+3.1}_{-2.6}$	(a)
log g	(dex)	5.25 ± 0.09	(a)
Age	(Gyr)	$7.0^{+2.8}_{-2.2}$	(b)
Distance	(pc)	$12.1616^{+0.0051}_{-0.0053}$	(c)
[m/H]	(dex)	-0.18 ± 0.05	(a)
[Fe/H]	(dex)	-0.24 ± 0.09	(a)
[O/H]	(dex)	-0.16 ± 0.05	(a)
[Na/H]	(dex)	-0.20 ± 0.09	(a)
[Mg/H]	(dex)	-0.41 ± 0.06	(a)
[Si/H]	(dex)	-0.14 ± 0.16	(a)
[K/H]	(dex)	-0.25 ± 0.09	(a)
[Ca/H]	(dex)	-0.25 ± 0.09	(a)
[Ti/H]	(dex)	-0.33 ± 0.08	(a)
[Cr/H]	(dex)	-0.20 ± 0.05	(a)
[Mn/H]	(dex)	-0.16 ± 0.08	(a)
$P_{\rm rot}$	(d)	~ 85	(a), (d)
$\langle \log R'_{\rm HK} \rangle$	–	$-5.62^{+0.10}_{-0.14}$	(a)

Note. (a) This work, (b) S. Dholakia et al. (2024), (c) C. A. L. Bailer-Jones et al. (2021), and (d) M. Kuzuhara et al. (2024).

The stellar elemental abundances for Gliese 12 were derived following the methodology of N. Gromek (2025), based on the work of N. Hejazi et al. (2023), and are also summarized in Table 3. We performed a spectral synthesis analysis using the 1D telluric-corrected CARMENES template spectrum. Synthetic spectra were generated with MARCS (Model Atmospheres with a Radiative and Convective Scheme) stellar atmosphere models (B. Gustafsson et al. 2008) and the TURBOSPECTRUM radiative transfer code (R. Alvarez & B. Plez 1998; B. Plez 2012), implemented via modified ISPEC routines (S. Blanco-Cuaresma et al. 2014; S. Blanco-Cuaresma 2019) using solar abundances from M. Asplund et al. (2009). The stellar parameters adopted to generate the model spectra were $T_{\rm eff} = 3328 \pm 78$ K, log $g = 5.00 \pm 0.05$ dex, [m/H] $= -0.30 \pm 0.11$ dex, $v_{\rm mac} = 5.0 \pm 1.0$ km s^{-1}, and $v_{\rm mic} = 0.5 \pm 0.5$ km s^{-1}. Of these parameters, $T_{\rm eff}$ and [m/H] were taken directly from the results of the STEPARSYN analysis, with log g calculated using the new mass and radius values. The macroturbulence and microturbulence velocities were determined by performing a χ^2-minimization over molecular OH lines, which are especially sensitive to these broadening parameters (D. Souto et al. 2017; N. Hejazi et al. 2023). Candidate absorption lines were selected from the normalized spectrum and cross-referenced with atomic and molecular features in the VALD (Vienna Atomic Line Database) line list (F. Kupka, M. L. Dubernet & VAMDC Collaboration 2011). The line list was further refined via visual inspection to exclude blended or contaminated features. The oxygen abundance was calculated using OH molecular features in place of O I lines.

For each spectral line, we generated a grid of synthetic spectra by varying the elemental abundance, [X/H], between −0.75 and +0.75 dex in steps of 0.25 dex, followed by interpolating the model spectra to a finer grid with 0.015 dex resolution. Best-fitting abun-

[6] https://github.com/mzechmeister/serval
[7] https://github.com/hmtabernero/SteParSyn/

dances were determined for each line via χ^2-minimization between the model and observed spectrum within a fitting window. The final abundances for each element are calculated via a weighted average of the individual abundances for each spectral line, with the weighting for each line equal to the root mean square error between the best-fitting model and the observed line in each line region, divided by the line depth. The uncertainties due to scatter ($\sigma_{\rm rms}$) were calculated as the standard deviation of the line-by-line abundance distribution divided by $\sqrt{N}$, where N is the number of lines used per element. Systematic uncertainties due to $T_{\rm eff}$, [m/H], $\log g$, $v_{\rm mac}$, and $v_{\rm mic}$ were estimated by independently resampling each stellar parameter from its Gaussian uncertainty distribution and repeating the full analysis over 15 iterations (N. Hejazi et al. 2023). The total uncertainty for each elemental abundance was computed by summing the random and systematic components in quadrature. Using the final abundances, we recomputed the global metallicity and α-enhancement of Gliese 12 following the prescription of N. R. Hinkel, P. A. Young & C. H. Wheeler (2022). By adding the number ratios of the available metals (O, Na, Mg, Si, K, Ca, Ti, Cr, Mn, and Fe), we find an overall metallicity of [m/H] $= -0.18 \pm 0.05$ dex, consistent with the metallicity reported by E. R. Newton et al. (2014), who determined an [Fe/H] of -0.17 ± 0.13 dex.

3.2 Stellar variability

Gliese 12 is overall a very quiet star as evidenced by its low $\langle \log R'_{\rm HK} \rangle$ value, a low X-ray flux, and low variability in the photometry. We recalculated the $\langle \log R'_{\rm HK} \rangle$ from the HARPS-N spectra and following the expressions of N. Astudillo-Defru et al. (2017). We found that over the timespan of the data, $\langle \log R'_{\rm HK} \rangle = -5.62$. Using the estimated relation between $\langle \log R'_{\rm HK} \rangle$ and the rotation period from N. Astudillo-Defru et al. (2017), the median rotation period is predicted to be ∼75 d.

We attempted to determine the stellar rotation period of Gliese 12 using long-term, ground-based photometric data from ASAS-SN, LCOGT, TJO, and E-EYE (see Fig. A1). Each data set was analysed independently – except for the E-EYE data, which included simultaneous V and R observations on the same nights – to assess whether they yielded consistent estimates of $P_{\rm rot}$. To model the photometric time-series, we fitted a linear function to account for long-term trends, alongside a sinusoidal function:

$$f(t) = z + mt + A \sin\left(\frac{2\pi t}{P_{\rm rot}} + \phi\right). \quad (1)$$

Here, t denotes the epoch of the photometric measurements. The free parameters include z and m, the coefficients of the linear trend, and the sinusoidal components: amplitude A, rotation period $P_{\rm rot}$, and phase ϕ. To account for correlated noise present in the data, we employed GPs (e.g. C. Rasmussen & C. Williams 2010; N. P. Gibson et al. 2012), specifically using an exponential kernel implemented in CELERITE[8] (D. Foreman-Mackey et al. 2017). We ran PYDE[9] to find optimal initial solutions, followed by a Markov chain Monte Carlo analysis with EMCEE (D. Foreman-Mackey et al. 2013) to determine posterior distributions (50 chains, 2×10^4 iterations with a thin factor of 100). Final parameter values were derived from these, using the median and 1σ percentiles.

The derived $P_{\rm rot}$ values are listed in Table 4. Our results indicate a relatively long stellar rotation period, with most estimates falling in the 80–90 d range. The most precise determination comes from the ASAS-SN g' data, yielding $P_{\rm rot} = 84.9^{+0.4}_{-0.3}$ d, consistent with the rotation period obtained by M. Kuzuhara et al. (2024) with ASAS-SN data. Rotation periods derived from V- band photometry are considerably less well determined.

[8] https://celerite.readthedocs.io/en/stable/
[9] https://github.com/hpparvi/PyDE

Table 4. Stellar rotation estimates from long-term photometry.

Facility	Photometric band	Value
ASAS-SN	V	$P_{\rm rot} = 80.3^{+23.9}_{-59.8}$ d
ASAS-SN	g'	$P_{\rm rot} = 84.9^{+0.4}_{-0.3}$ d
LCOGT	B	$P_{\rm rot} = 92.7^{+4.8}_{-2.9}$ d
LCOGT	V	$P_{\rm rot} = 86.6^{+22.3}_{-32.5}$ d
TJO	R	$P_{\rm rot} = 77.0^{+1.9}_{-1.9}$ d
E-EYE	V, R	$P_{\rm rot} = 81.8^{+3.3}_{-3.2}$ d

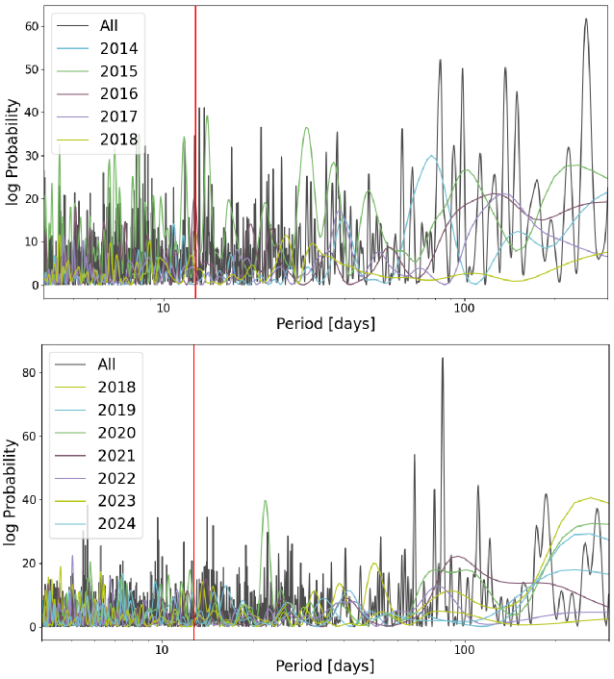

Figure 2. BGLS periodogram of the ASAS-SN V-band (top) and g'-band (bottom) data of Gliese 12, of the full data and per season. The red vertical line indicates the planet period.

Applying a Bayesian Generalised Lomb-Scargle (BGLS) periodogram (A. Mortier et al. 2015) to the ASAS-SN data and splitting the data into the different observing seasons, we found that, unsurprisingly, the variability is season-dependent with several years showing no variability around 80 d across both photometric bands. The periodogram is shown in Fig. 2. It confirms that this star is relatively quiet and that the variability pattern is not clear-cut. We caution that this may contribute to having the rotation periods better or less well determined above as it will partly depend on the seasons when the photometry was taken.

Finally, we looked at the discrete correlation function (DCF) between Hα and RVs. Since these are measured from the same spectra and available for all our spectroscopic data sets, they could be used in a multidimensional GP regression fit. We applied the algorithm from R. A. Edelson & J. H. Krolik (1988) to compute the DCF. The resulting analysis shows that Hα and RVs are mildly anticorrelated and that there is a small timeshift of about 10 d. This

can again point to a rotation period of 80 d where any time-shift expresses itself at about one-eighth of the rotation period (A. Collier Cameron et al. 2019; A. Mortier 2022). Perhaps more intriguingly, the data become mildly correlated after 50–70 d (depending on the direction of the time shift). This points to a rotational correlation time-scale between Hα and RV of 120 d. While this is unlikely to be the rotational period considering the alternative measurements, it appears to be the time-scale manifested in the data that we have. As seen later in Section 5, several values are identified for the GP rotational periodicity parameter when applying a wide GP prior, including 80 and 120 d. The mass of the planet is not affected by this choice.

4 PHOTOMETRY MODELLING

We fit the available photometry from *TESS*, *CHEOPS*, and MuSCAT2/3 jointly in JULIET (N. Espinoza et al. 2019). We used the six detrended *CHEOPS* visits that contain a transit of Gliese 12 b as well as the five *TESS* sectors, and four detrended MuSCAT2/3 observations across r, i, and z bands. In order to detrend the *TESS* data, we included a GP with the approximate Matérn kernel implemented into JULIET with CELERITE (D. Foreman-Mackey et al. 2017; fitting for the amplitude of the GP, GP_σ, and the time-scale of the GP, GP_ρ). We fit for:

the period, P;
the time-of-transit centre, T_0;
the planet-to-star radius ratio, $R_{\rm pl}/R_\star$;
the impact parameter, b;
the stellar density, ρ;
the limb darkening coefficients parametrized following D. M. Kipping (2013), for *TESS*, *CHEOPS*, and MuSCAT2/3 r, i, and z bands, respectively;
the jitter, for *TESS*, *CHEOPS*, and MuSCAT2/3 r, i, and z bands, respectively;
the offset relative flux, for *TESS*, *CHEOPS*, and MuSCAT2/3 r, i, and z bands, respectively.

Due to the isolated field, we fixed the dilution factor for *TESS*, *CHEOPS*, and MuSCAT2/3 r, i, and z bands to 1. We used the values for the period and time-of-transit centre derived from M. Kuzuhara et al. (2024) as priors in a normal distribution but inflated the width to be 0.1. We also set a normal distribution for the stellar density with the stellar values obtained from M. Kuzuhara et al. (2024). We let the other parameters vary uniformly. All the prior distributions are listed in Tables C1 and C2.

Finally, we performed two different fits, one assuming a circular orbit and one with free eccentricity and argument of periastron. Both fits resulted in higher precisions on the period and time-of-transit centre as compared to S. Dholakia et al. (2024) and M. Kuzuhara et al. (2024). Furthermore, the additional *TESS* sector and *CHEOPS* visit as well as the re-extraction of the *CHEOPS* data, and joint fitting with the MuSCAT2/3 photometry allows us to derive the planet radius from the fit more precisely. From the circular fit, we found a radius of $0.96 \pm 0.03\,\mathrm{R}_\oplus$, while the eccentric solution gave a radius of $0.90 \pm 0.04\,\mathrm{R}_\oplus$ with an eccentricity of $0.39^{+0.17}_{-0.11}$.

We adopted the eccentric fit as our final result. We show the phase-folded transits with the best-fitting model from JULIET in Fig. 3. Final extracted values for the orbital and planetary parameters are listed in Table 5 and the stellar and instrumental parameters are listed in Table C3.

5 RV MODELLING

We fitted the RVs (HARPS-N `S-BART`, ESPRESSO `S-BART`, and CARMENES `SERVAL`) using the PYANETI package,[10] presented by O. Barragán, D. Gandolfi & G. Antoniciello (2019); and O. Barragán et al. (2022). Within a periodogram of the RV data (see Fig. B1), the signal of the planet is not apparent to any significance. However, since the orbital period and time of transit are known from photometric modelling, we used these results to inform the corresponding priors for this RV fit. Despite the small value of $\log R'_{\rm HK}$, as shown in Table 3, there are also signs in the periodogram of possibly stellar-related signals in the data that manifest as peaks in the long-period regime (see Fig. B1).

We used PYANETI as it is one of few packages that can model the RVs with a single GP, but it can also do multidimensional GP fitting, where multiple data sets are comodelled with one common GP (V. Rajpaul et al. 2015; O. Barragán et al. 2022). We used both functionalities when modelling the RVs, and also tried fitting without any GP at all. In all cases where a GP was used, we employed the quasi-periodic kernel and fit for the GP amplitudes (A_0 for the single GP and adding in A_1 and A_2 for the multi-GP), the activity decay time-scale ($\lambda_{\rm e}$), the inverse harmonic complexity ($\lambda_{\rm p}$), and the stellar rotation period ($P_{\rm rot,GP}$); see V. Rajpaul et al. (2015) and O. Barragán et al. (2022) for a more detailed description of the kernel.

In all fits, the eccentricity, e, and argument of periastron, ω, were reparametrized as $\sqrt{e}\sin\omega$ and $\sqrt{e}\cos\omega$, as in J. Eastman, B. S. Gaudi & E. Agol (2013). As aforementioned, the orbital period, P, and transit time, T_0, were fit with Gaussian priors, informed by the results of the photometry-only fit; the prior on T_0 was adjusted (accounting for the uncertainty in P) to ensure that it fell near the midpoint of the RV data. Finally, offsets and jitter corresponding to the individual instruments were also fitted as free parameters in the models.

A multitude of runs were performed, including circular and eccentric models; no GP, single GP, and multidimensional GPs. For the latter, various combinations of parameters (i.e. FWHM, BIS, and Hα) were utilized in combination with the RVs. The rotation period prior was varied, allowing for a wide prior, a prior centred around 80 d motivated by the photometry, and a prior centred around 120 d motivated by the results of the wide prior and the coherence time-scale between the RVs and the Hα indicator from the DCF analysis. All results constrain the planet parameters similarly and they are all consistent within less than 0.5σ. Several results are virtually indistinguishable for the planet parameters, but the BIC values show preference for the model with a GP applied to the RVs with $\Delta\mathrm{BIC} = 77.9$ compared to the next-best model (no GP). We decided to adopt the results achieved from the model using a standard GP applied solely to the RV data, as the BIC values show preference for this model. All prior distributions of the adopted fit can be found in Tables C1 and C2.

We measured an RV semi-amplitude of $K = 0.70\,\mathrm{m\,s^{-1}}$ with a 3.6σ significance. The phase-folded model and data are presented in Fig. 4. We thus found that Gliese 12 b has a mass of $0.98^{+0.27}_{-0.28}\,\mathrm{M}_\oplus$, and an eccentricity of $0.24^{+0.15}_{-0.12}$ constrained only at the 2σ level. With the current data set, we were not able to more-precisely constrain the eccentricity. Upon checking all the individual results, high consistency on the planet parameters was found between runs where parameters agreed well within 0.5σ. For some runs, this is shown in Fig. 5.

[10] https://github.com/oscaribv/pyaneti

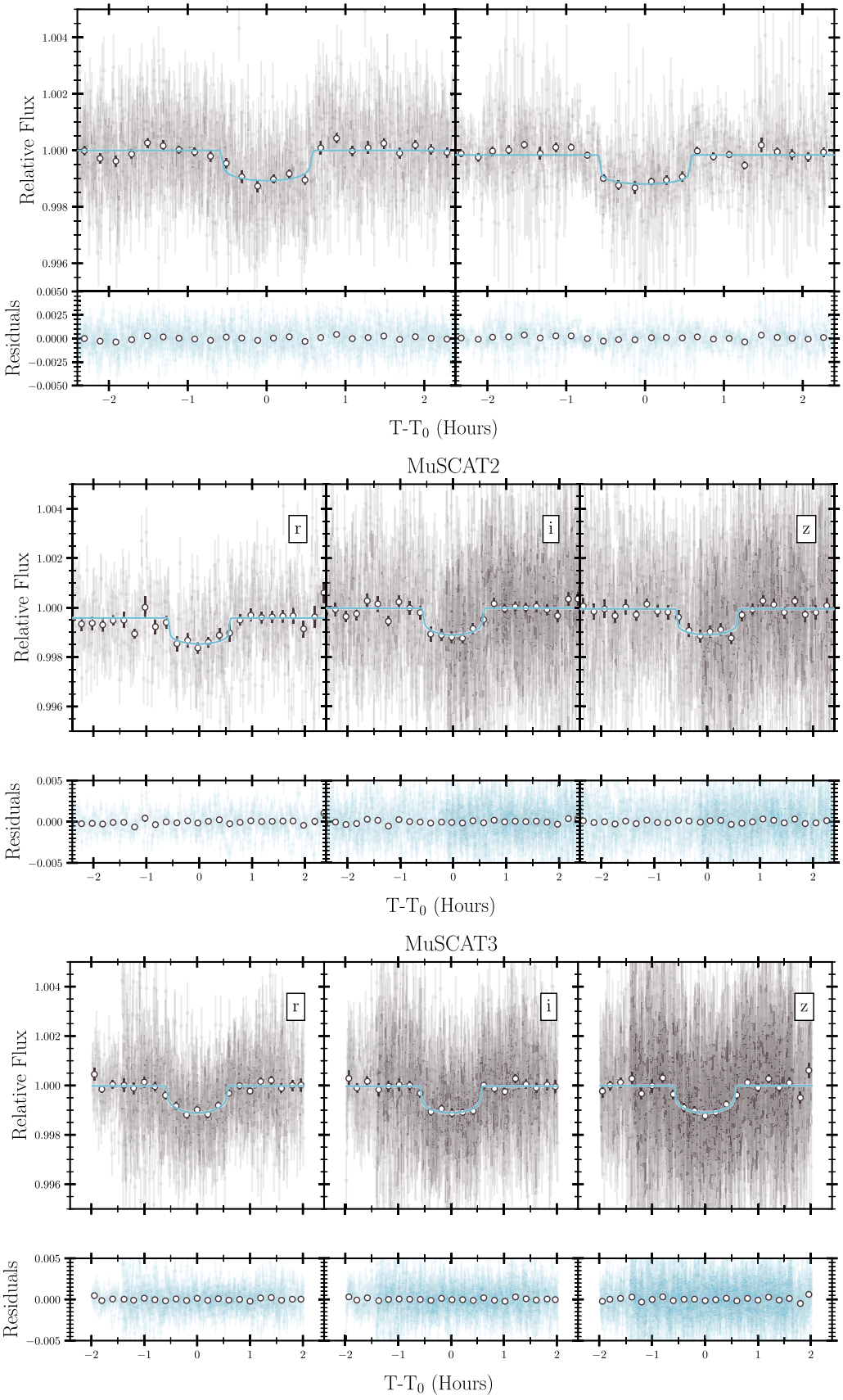

Figure 3. Detrended and phase-folded transits of Gliese 12 b with the best-fitted model from JULIET overlaid in blue as well as the residuals on the bottom. Top left: *TESS*; top right: *CHEOPS*, middle: MuSCAT2; and bottom: MuSCAT3.

Table 5. Gliese 12 b orbital and planetary parameters for the three different fitting procedures. The fitted parameters are above the horizontal line and the derived parameters below. Exceptions are mentioned in the notes below the table.

Parameter	Unit	Photometry-only	Informed RV fit	Joint fit
P	(d)	$12.761417^{+0.000047}_{-0.000037}$	12.761421 ± 0.000047	$12.761418^{+0.000060}_{-0.000055}$
T_0	(BJD)	$2459497.1855^{+0.0020}_{-0.0026}$	$2460492.5745^{+0.0045}_{-0.0043}$	$2460033.16351^{+0.00087}_{-0.00088}$
$R_p/R_\star$	–	$0.03080^{+0.00084}_{-0.00073}$	–	$0.0323^{+0.0015}_{-0.0014}$
b	–	$0.51^{+0.12}_{-0.12}$	–	$0.75^{+0.09}_{-0.15}$
$\rho_\star$	($g\,cm^{-3}$)	$19.211^{+1.183}_{-1.198}$	–	$19.518^{+2.812}_{-2.766}$
K	($m\,s^{-1}$)	–	$0.70^{+0.19}_{-0.20}$	$0.67^{+0.21}_{-0.21}$
$\sqrt{e}\sin\omega$	–	–	$-0.12^{+0.38}_{-0.33}$	$-0.09^{+0.40}_{-0.33}$
$\sqrt{e}\cos\omega$	–	–	$0.35^{+0.12}_{-0.20}$	$0.35^{+0.12}_{-0.24}$
e	–	$0.39^{+0.17}_{-0.11}$	$0.24^{+0.15}_{-0.12}$ (< 0.53)	$0.24^{+0.13}_{-0.13}$ (< 0.46)
ω	(deg)	143^{+28}_{-39}	-18^{+61}_{-41}	-16^{+68}_{-41}
$a/R_\star$	–	$54.9^{+1.1}_{-1.2}$	–	$55.2^{+2.5}_{-2.7}$
i	(deg)	89.47 ± 0.13	–	$89.25^{+0.08}_{-0.09}$
M_p	($M_\oplus$)	–	$0.98^{+0.27}_{-0.28}$	$0.95^{+0.29}_{-0.30}$
R_p	($R_\oplus$)	$0.90^{+0.04}_{-0.03}$	–	$0.93^{+0.06}_{-0.06}$
ρ_p	($g\,cm^{-3}$)		$7.0^{+2.3}_{-2.1}$	6.4 ± 2.4

Note. For the photometric fit, e and ω are fitted directly; in the informed RV and the joint fit, they are derived. Numbers in brackets indicate the 2σ upper limit for the value.

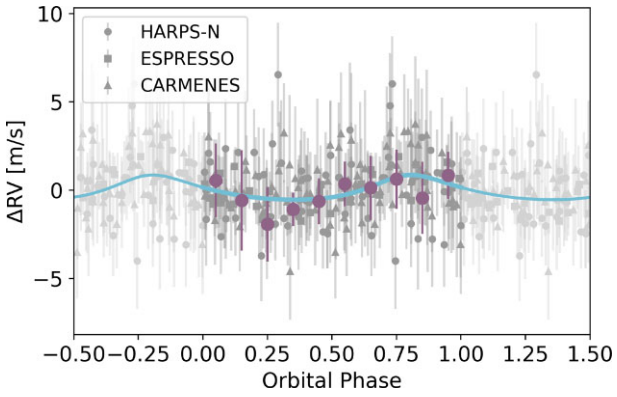

Figure 4. Phase-folded RVs from the best-fitted informed RV model with GPs removed. Binned data shown by the large, purple points (10 bins). Phase-folded on the period of the planet (12.761421 d).

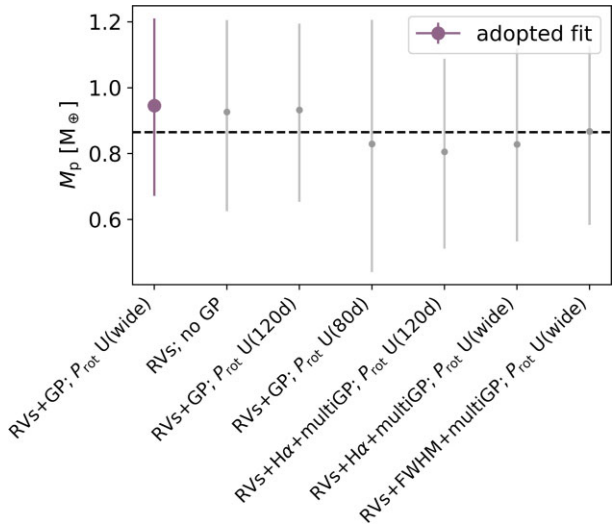

Figure 5. A summary of the variety of models fitted to the RV data. The large purple point highlights the adopted fit. Here, $\mathcal{U}$(wide) indicates wide uniform priors for the GP period (as in Table C2), and $\mathcal{U}$(value) indicates uniform priors defined with 15 d either side of the specified value. The dashed, black line indicates the weighted mean of all the mass values.

It is recognized that the period of the GP does not always converge at the value of the rotational period that was identified via photometry (85 d). Additionally, constraining the GP period of around 85 d resulted in a poorer fit in comparison to a wider prior. Given that $\langle \log R'_{HK} \rangle = -5.62$, it is suspected that Gliese 12 is too quiet to confidently ascertain the rotational period using RV data alone. GP-free, multi-Keplerian fits were also run as discussed in Section 7.5.

6 JOINT PHOTOMETRY AND RV MODELLING

We used PYORBIT[11] (L. Malavolta et al. 2016, 2018) to perform a joint fit of the space-based transit observations, RVs, and the spectroscopic activity index Hα. We deliberately excluded the ground-based MuSCAT2 and MuSCAT3 photometry from the analysis, as incorporating them significantly increases the computational cost of the fit. More importantly, ground-based light curves are often affected by systematics, such as atmospheric effects, airmass trends, and instrumental noise. These systematic effects can introduce biases in the determination of transit depths, particularly for shallow transits like this one. In contrast, space-based observations offer higher photometric stability and precision, making them more reliable for this kind of analysis. Transit modelling was carried out using PYTRANSIT[12] (H. Parviainen 2015), and the red noise in each light curve was accounted for using GPs with a Matérn 3/2 kernel.

The RV systematics were also modelled using GPs, with selected hyperparameters shared with those used for the Hα spectroscopic activity index in order to account for stellar activity. We selected

[11] https://github.com/LucaMalavolta/PyORBIT

[12] https://github.com/hpparvi/PyTransit

Hα as the preferred activity indicator because its GLS periodogram (M. Zechmeister & M. Kürster 2009) showed a prominent peak near the stellar rotation period derived from ground-based photometry. We adopted a quasi-periodic with cosine (QPC) kernel (M. Perger et al. 2021), where the characteristic period ($P_{\rm rot}$), the active-region decay time-scale (λ), and the coherence scale (w) were modelled as common (and free) hyperparameters across both the RV and Hα data sets. Although we possessed an independent estimate of the stellar rotation period based on long-term photometric monitoring, we imposed a uniform prior on $P_{\rm rot}$ in the range [60 d, 200 d] in order to assess whether the GP model could recover the photometric value without direct constraint and due to the seasonal variability found in the photometry.

To speed up the analysis, we limited the *TESS* data to 12-h time windows centred on the predicted mid-transit times. For both the *TESS* and *CHEOPS* transit light curves, the following parameters were fitted: the central time of transit (T_0), orbital period (P), eccentricity (e), and argument of periastron (ω), using the parametrization from J. Eastman et al. (2013) ($\sqrt{e}\sin\omega$, $\sqrt{e}\cos\omega$). We also fitted the quadratic limb-darkening coefficients (u_1, u_2) independently for each instrument, constrained by normal priors based on predicted values from LDTK[13] (T. O. Husser et al. 2013; H. Parviainen & S. Aigrain 2015), as well as the impact parameter (b) and the planet-to-star radius ratio ($R_{\rm p}/R_\star$). We also fitted the stellar density ($\rho_\star$) using a normal prior based on the stellar parameters presented by M. Kuzuhara et al. (2024). Each light curve included a white noise term as an additional free parameter.

For the RV data, we included instrument-specific offsets and jitter terms as free parameters in the model. In addition to these offsets, we fitted for P, e (using the parametrization $\sqrt{e}\sin\omega$, $\sqrt{e}\cos\omega$), and K. As described above, several GP hyperparameters were shared between the RV and Hα time-series. Specifically, the kernel amplitude (H) and the amplitude of the cosine component (C) were fitted independently for each time-series, while $P_{\rm rot}$, λ, and w were treated as common parameters and fitted jointly.

The joint fit was performed in two stages. First, we applied global optimization of the parameters using PYDE. Starting from the optimal solution, the parameter space was subsequently explored using EMCEE, running for 2.5×10^6 iterations to meet the convergence criteria of PYORBIT. The final fitted orbital and planetary parameters and corresponding priors are listed in Table 5 and Table C1, respectively. Similarly, the stellar and instrumental priors and resulting values are listed in Tables C2 and C3.

Our joint fit yields results for Gliese 12 b that are consistent with those obtained from the photometry-only and informed RV analyses. The simultaneous modelling of the RVs and the Hα activity index using the QPC kernel produced a rotation period of $P_{\rm rot} = 172.0^{+1.5}_{-1.6}$ d. This value is close to twice the rotation period inferred from long-term photometry ($P_{\rm rot} \sim 85$ d). We note that $P_{\rm rot}$ here refers to the characteristic period recovered by the GP model and is not necessarily the stellar rotation period itself. The QPC kernel, as described by M. Perger et al. (2021), is designed to account for quasi-periodic signals at both $P_{\rm rot}$ and its first harmonic ($P_{\rm rot}/2$), which commonly arise due to spot configurations that produce symmetric signals that repeat every half rotation. In this context, the fitted period of ∼172 d probably corresponds to the harmonic of a true rotation period near 85 d. Tests using the QPC kernel on the RV and Hα data sets separately confirm that the kernel can recover the 85-d period when a uniform prior in the range [60 d, 100 d] is adopted for $P_{\rm rot}$. A stellar rotation period significantly longer than 100 d appears unlikely, as such long periods are rare among M dwarfs (see E. R. Newton et al. 2016; Y. Shan et al. 2024). We therefore consider a rotation period close to 85 d as the more physically plausible scenario for Gliese 12.

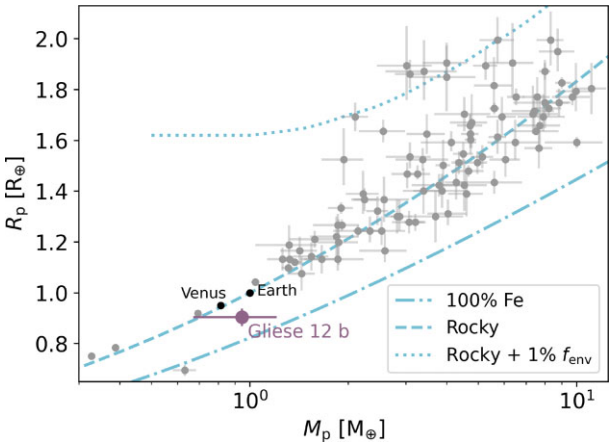

Figure 6. Mass–radius diagram of all small planets ($R_{\rm p} \leq 2\,R_\oplus$) in the PlanetS database (small, grey), Earth and Venus (labelled, black), and Gliese 12 b (large, purple). The 100 per cent Fe and rocky compositional lines are taken from L. Zeng et al. (2019), and the rocky + 1 per cent $f_{\rm env}$ line is from H. Chen & L. A. Rogers (2016).

7 DISCUSSION

All the orbital and planetary parameters are consistent across the different fits. For the upcoming discussion of Gliese 12 b, we adopted as final parameters the values from the joint fit. Thanks to our extensive RV campaign, we now have the first definitive mass for Gliese 12 b. Having both a precise radius and mass allows for an in-depth study of a planet that is not possible without a mass measurement, see N. E. Batalha et al. (2019); and J. A. Egger et al. (2024). A bulk density can be obtained, which in turn can say something about the type of planet Gliese 12 b is and how that compares with other currently known exoplanets. We can also go one step further and infer the possible interior composition of Gliese 12 b as well as the possibility of it having an atmosphere. We investigate all of this in the upcoming sections. Finally, we examine the data for evidence of additional, detectable planets in the system.

7.1 Gliese 12 b as an exo-Venus

Gliese 12 b occupies a unique region of parameter space due to its distinctive physical properties. For comparison reasons, we used the well-curated PlanetS database (L. Parc et al. 2024) maintained on the DACE platform.[14] We further limited it to all planets with a radius less than $2\,R_\oplus$. Fig. 6 shows the mass–radius diagram of this sample of small planets. It is directly obvious that Gliese 12 b lies in the same part of parameter space as Earth and Venus with a radius closer to Venus. Its density makes it marginally denser than our rocky Solar system planets.

The orbital period of Gliese 12 b is much smaller than those of Earth and Venus. However, since the host star is an M dwarf, Gliese 12 b is actually a temperate planet, too. We have calculated

[13] https://github.com/hpparvi/ldtk

[14] https://dace.unige.ch/exoplanets/

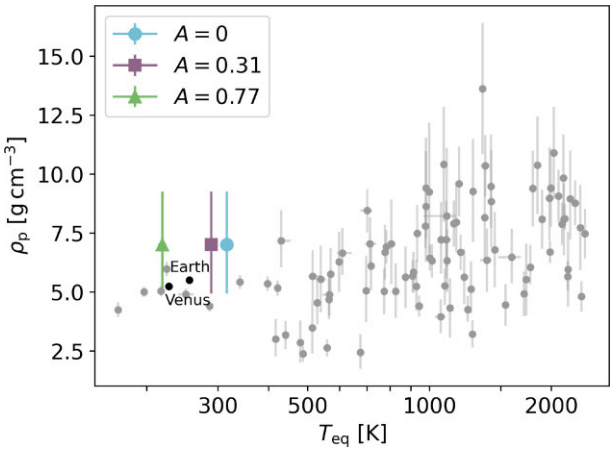

Figure 7. Planetary density versus equilibrium temperature for the same sample of planets as in Fig. 6. For Gliese 12 b, different Bond albedo values were used: $A = 0$, Earth's albedo ($A = 0.31$), and Venus' albedo ($A = 0.77$). The small, unlabelled planets in grey are those from the PlanetS database, with the TRAPPIST-1 planets lying in a similar region to Gliese 12 b.

$T_{\rm eq}$ following N. B. Cowan & E. Agol (2011). As the albedo is unknown, we have to make an assumption. We calculated $T_{\rm eq}$ three times, using a Bond albedo of 0, as well as both Earth's and Venus' albedo (0.31 and 0.77 respectively). We found that the $T_{\rm eq}$ of Gliese 12 b is between 317 and 219 K. When using Venus' albedo, the $T_{\rm eq}$ of Gliese 12 b is extremely close to that of Venus itself. Combined with the more Venus-like radius, we could conclude that this planet is possibly Venus-like.

Fig. 7 shows the different positions of Gliese 12 b on a planet density versus equilibrium temperature diagram. We caveat that different albedos may have been used for the PlanetS database. In any case, whichever the true $T_{\rm eq}$, Gliese 12 b occupies a sparsely populated area in this parameter space, making it a truly remarkable characterized exoplanet. The only well-characterized ($\sigma_{R_{\rm p}} \leq 8$ per cent; $\sigma_{M_{\rm p}} \leq 25$ per cent) planets that also occupy a similar region in parameter space are LHS 1140 b (C. Cadieux et al. 2024), a super-Earth characterized by ESPRESSO, and the TRAPPIST-1 (Transiting Planets and Planetesimals Small Telescope) planets (M. Gillon et al. 2017; E. Agol et al. 2021) where mass measurements come from transit timing variations.

As its host star is also one of the closest known planet host stars, there are plenty of opportunities for continued follow up of this exo-Venus. Additional information on atmospheric properties, and further and deeper characterization of the system will reveal how similar (or discrepant) Gliese 12 b is from Venus itself.

7.2 Interior composition modelling

Having a planetary mass and radius for Gliese 12 b, we calculated a mean bulk density of $6.4 \pm 2.4\,{\rm g\,cm^{-3}}$, suggesting it is ever so slightly denser than Earth and Venus. We can also model the possible interior compositions for this small planet. For this purpose, we used the publicly available interior modelling code PLANETIC[15] (J. A. Egger et al. 2024). This framework utilizes a neural network that was trained on the BICEPS forward model (J. Haldemann et al. 2024), combined with a full grid accept–reject sampling scheme. PLANETIC has been shown to be fast as well as reliable when characterizing the possible interior compositions of small planets.

Within PLANETIC, a planet can have up to three layers: an inner core made of iron (Fe) and sulphur (S), a rocky mantle composed of oxidized silicon (Si), magnesium (Mg), and Fe, and a volatile layer uniformly mixed between water and pure hydrogen–helium. It thus does not have a separate water layer.

We assumed in the model that the planet formed outside the ice line since a H/He envelope as expected from a formation within the ice line would not be stable against evaporation as shown in Section 7.3 and all water was thus accreted in the form of ice (see J. A. Egger et al. 2024, for more detail). Although we cannot rule out the possibility of an *in-situ* formation, we model the interior of Gliese 12 b based on the above assumption as a demonstration. Since Gliese 12 b is either a bare core planet or has a high mean molecular weight envelope, we model this planet with the water-rich prior in PLANETIC.

Different compositional priors can further be set based on the host star. There are preliminary studies showing possible links between host star and planet composition (e.g. A. Thiabaud et al. 2015; A. Mortier et al. 2020; V. Adibekyan et al. 2021). However, the exact link is still unknown, which is why PLANETIC allows for the different priors. The relevant priors relate to the Si/Mg/Fe ratios. They can be sampled uniformly, have a prior where the planet ratios are assumed to be equal to the star's (A. Thiabaud et al. 2015), or have a prior assuming the planet is iron-enriched compared to the star as described by equation (S5) of V. Adibekyan et al. (2021). Within PLANETIC, abundances are recorded in the form $10^{[{\rm X/Fe}]_\star}$ in the posteriors, allowing us to compare the abundance priors, which are 0.88 ± 0.25 and $0.30^{+0.21}_{-0.11}$ for X=Si, and 0.79 ± 0.19 and $0.27^{+0.17}_{-0.09}$ for X=Mg for the equal and iron-enriched prior respectively. We used the stellar abundances derived in Section 3 as priors, where we used Ti as a reliable proxy for Si. The quality of silicon lines for stars with temperatures similar to that of Gliese 12 becomes degraded in comparison to the quality in hotter stars, in which case, the silicon value may be erroneous. The use of Ti as a proxy is justifiable due to it being an alpha element, as is Si; both elements form via the same process during stellar nucleosynthesis, and should therefore follow similar trends in abundances. We selected Ti in particular as there are many resolvable lines, amenable to analysis.

The resulting mass fractions of the different layers are shown in Fig. 8. As expected for this planet, the volatile mass fraction is small and consistent with 0. The core mass fraction is loosely constrained with median values between 20 and 30 per cent, depending on the prior. This is in line with the known core mass fraction of Venus (32 per cent).

7.3 Atmospheric mass loss

Gliese 12 b is also an intriguing target for transmission spectroscopy in the Lyman-α line. Lyman-α observations can reveal escaping hydrogen gas during exoplanet transits (A. Vidal-Madjar et al. 2003), but interstellar absorption and geocoronal emission often obscure the line core, leaving observations to be sensitive only in the high-velocity line wings (e.g. D. Ehrenreich et al. 2015). Nearby systems with high systemic RVs offer both higher flux and weaker interstellar absorption, and offset the interstellar absorption line core from the stellar emission line core. This allows to reveal information content at lower velocities and these targets are thus ideal for these studies.

At a distance of 12.2 pc and a systemic velocity of $51.2\,{\rm km\,s^{-1}}$, the Gliese 12 system satisfies both of these criteria. Using the serendipitous detection of X-ray emission from Gliese 12 by *XMM–*

[15] https://github.com/joannegger/plaNETic

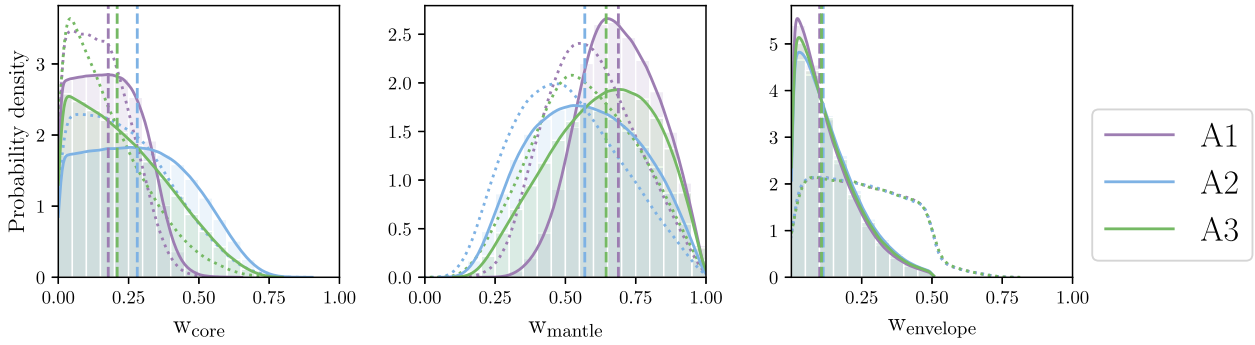

Figure 8. Posterior distributions (solid lines) of the interior structure of Gliese 12 b, showing, from left to right, the mass fractions of the inner core, mantle, and volatile components. The different colours represent the three different priors for the planetary Si/Mg/Fe ratios: stellar (purple, A1), iron-enriched (blue, A2), and uniform (green, A3). Dotted lines indicate the priors and vertical dashed lines show the median of each posterior distribution.

Newton ($F_X = 6.8 \pm 2.4 \times 10^{-15}$ erg cm^{-2} s^{-1}; N. A. Webb et al. 2020) and the J. L. Linsky, K. France & T. Ayres (2013) relation between Lyman-α and X-ray flux, we expected Gliese 12 to have an intrinsic Lyman-α flux of 1.1×10^{-13} erg cm^{-2} s^{-1}. Based on the modest column density of neutral hydrogen predicted by the Colorado Local Interstellar Medium (LISM) model (S. Redfield & J. L. Linsky 2000) of $N_H = 1.1 \times 10^{18}$ cm^{-2} and the high systemic RV, we expected Gliese 12 b to be a suitable target for Lyman-α transmission spectroscopy. It will soon be observed for this purpose by *HST* GO 17 600 (PI: Vissapragada).

We additionally simulated the past evaporation history of Gliese 12 b in order to determine whether an H/He-rich envelope would have survived to the present day under X-ray irradiation from its host star. To do so, we adopted the PHOTOEVOLVER code (J. Fernández Fernández, P. J. Wheatley & G. W. King 2023), which combines three components to simulate the evaporation history of close-in exoplanets; these are (1) a model of the X-ray emission history of the host star, (2) an envelope structure model that links the mass fraction of the H/He atmosphere to its thickness, and (3) a model for the atmospheric escape rate. Therefore, on each time-step, PHOTOEVOLVER computes the X-ray emission at the current simulation age using the X-ray emission model. Then, the corresponding incident X-ray flux of the planet is fed into the mass-loss model to obtain a mass-loss rate. The amount of mass lost during the time-step is then removed from the planet's gaseous atmosphere; and, finally, the envelope thickness is recalculated using the envelope structure model.

Regarding the X-ray emission history model, in Fig. 9 we compared the *XMM–Newton* detection of Gliese 12 with the X-ray luminosity–age relations by C. P. Johnstone et al. (2021), which were based on a rotational evolution model fitted to open clusters, and by S. G. Engle (2024), which were based on empirical fits to populations of M dwarfs.

At the age of Gliese 12 (see Tab. 3), the model by S. G. Engle (2024) predicted an X-ray luminosity of $3.0^{+10}_{-2.0} \times 10^{26}$ erg s^{-1} (energy range 0.1–2.5 keV), whilst the model by C. P. Johnstone et al. (2021) predicted $6.6^{+5.0}_{-2.0} \times 10^{26}$ erg s^{-1} in the same energy range. Additionally, M. Kuzuhara et al. (2024) presented *XMM–Newton* measurements of Gliese 12 and reported an X-ray luminosity of $6.0 \pm 1.3 \times 10^{25}$ erg s^{-1} (range 0.124–2.5 keV), which corresponds to $6.2 \pm 1.3 \times 10^{25}$ erg s^{-1} when extrapolated to the energy range of 0.1–2.5 keV used by the models above (using the *WebPIMMS* tool[16]).

[16]https://heasarc.gsfc.nasa.gov/Tools/w3pimms_help.html

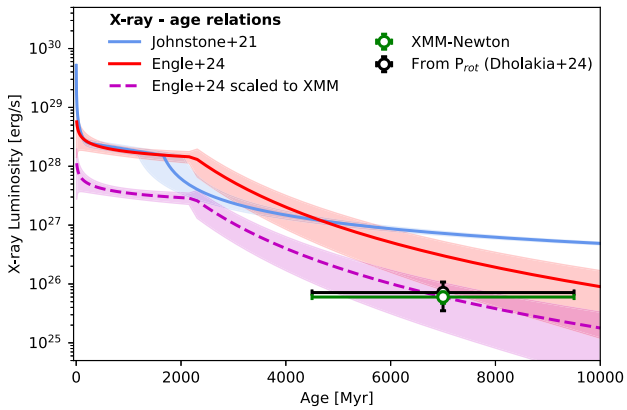

Figure 9. Comparison of several X-ray luminosity–age relations with the *XMM–Newton* observation of Gliese 12 (green circle). The plotted X-ray age relations are: C. P. Johnstone, M. Bartel & M. Güdel (2021, solid blue line), S. G. Engle (2024, solid red line), and the same model scaled down to fit the *XMM–Newton* measurement from M. Kuzuhara et al. (2024). The shaded regions correspond to the 1σ uncertainties in the models. The X-ray luminosity determined from the spin period measured by S. Dholakia et al. (2024) and the rotation-activity relation by S. G. Engle & E. F. Guinan (2023) is also shown (black circle) and is in very good agreement with the measured X-ray emission.

Overall, we found the model by S. G. Engle (2024) more consistent with the *XMM–Newton* X-ray luminosity presented by M. Kuzuhara et al. (2024), within a factor of 5, and thus we favoured it over the model by C. P. Johnstone et al. (2021), which is 11 times brighter. We additionally considered an alternative X-ray emission history for Gliese 12 where we scaled down the model by S. G. Engle (2024) to fit the *XMM–Newton* measurement presented by M. Kuzuhara et al. (2024).

We also considered the contribution from the stellar extreme ultraviolet (EUV) emission, which can have a significant impact on atmospheric escape on longer time-scales than X-ray alone (J. E. Owen & A. P. Jackson 2012; G. W. King et al. 2018; J. Sanz-Forcada et al. 2025). We adopted the X-ray–EUV relations by G. W. King et al. (2018) to compute the EUV emission history (13.6–100 eV) from the X-ray emission history models (0.1–2.5 keV) described above. In our simulations, we then considered the contribution from both the X-ray and EUV irradiation when computing the mass-loss history of the planet.

Regarding the envelope structure model, we adopted the models presented by H. Chen & L. A. Rogers (2016). They adapted the

MESA code (B. Paxton et al. 2011) to build mass–radius relations for gaseous atmospheres on planets from Earth-mass to Jupiter-mass. In this work, we adopted the polynomial fit that they performed to their simulation results (H. Chen & L. A. Rogers 2016, equation 5), valid for envelope mass fractions of 0.01–20 per cent and planet masses of 1–20 $M_\oplus$.

Finally, regarding the mass-loss model, we adopted the models presented by D. Kubyshkina et al. (2018), which accounts for both core-powered mass loss as well as energy-limited and recombination-limited escape from both X-ray and EUV photons, and is based on hydrodynamic simulations. In this work, we adopted the pre-computed grid of planet parameters and interpolation routine presented by D. I. Kubyshkina & L. Fossati (2021), valid for planet masses of 1–39 $M_\oplus$ and planet radii of 1–10 $R_\oplus$.

Motivated by its high density, we assumed that Gliese 12 b has no significant gaseous envelope at present. We then considered a number of initial envelopes on the planet, with mass fractions of 1 per cent, 2 per cent, and 5 per cent. We did not consider larger initial atmospheres as these would have been stripped off and truncated by boil-off processes shortly after dispersal of the protoplanetary disc (J. G. Rogers, J. E. Owen & H. E. Schlichting 2024).

We thus simulated the past evaporation history of Gliese 12 b in each scenario. Our PHOTOEVOLVER calculations adopted the fourth-order Runge–Kutta integration method with a maximum time-step of 1 Myr, in the interval between 10 Myr and 1 Gyr. Additionally, we considered the gaseous envelope to be fully stripped when it reaches a mass fraction below 0.01 per cent, which corresponds to the minimum value the envelope structure model by H. Chen & L. A. Rogers (2016) is rated for.

In Fig. 10, we show the results from our simulations, from 10 Myr to 10 Gyr. On the top panel, we show atmospheric evolution under the X-ray emission history predicted by S. G. Engle (2024, and its corresponding EUV emission history from the relations by G. W. King et al. 2018), and on the bottom panel, the atmospheric evolution under the same emission history, but scaled down by a factor of 5 to match the *XMM–Newton* observation of Gliese 12 as we do not know the true X-ray history of the star. We found that all H/He envelopes are fully stripped from Gliese 12 b within 150 Myr, with none surviving to the present day. Even with the faintest X-irradiation model, the envelope lifetime is only extended to the age of 200 Myr.

In our simulations, we neglected the contribution to atmospheric escape from additional mechanisms, such as stellar flares, coronal mass ejections, and magnetic interactions (e.g. A. A. Vidotto et al. 2013; D. Atri & S. R. C. Mogan 2021; G. Hazra et al. 2025). These mechanisms would only strengthen mass-loss rates, causing the planet's envelope to be lost even earlier in its life.

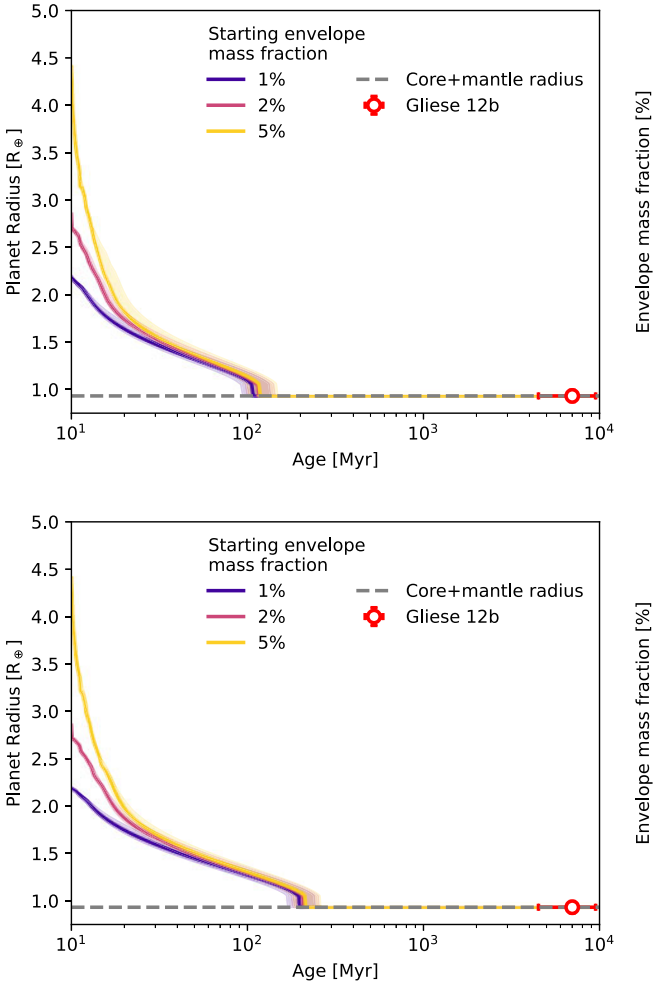

Figure 10. Top panel: evolution of the total radius (core + mantle + envelope) of Gliese 12 b under atmospheric escape using the X-ray irradiation history predicted by S. G. Engle (2024), with a range of initial atmospheres with mass fractions of 1 per cent (blue line), 2 per cent (red line), and 5 per cent (yellow line). The shaded regions correspond to possible evaporation histories taking into account the 1σ uncertainties in the planet's radius, mass, and X-ray irradiation history. The present-day total radius and age of Gliese 12 b is plotted as a red circle, and the size of its core and mantle as a dashed grey line. Bottom panel: evolution of the total radius (core + mantle + envelope) of Gliese 12 b under atmospheric escape, following the top panel, using the X-ray irradiation history predicted by S. G. Engle (2024) scaled down by a factor of 5 to match the *XMM–Newton* observation.

7.4 Prospects for atmospheric characterization

Given its high mean density and the intense XUV irradiation from its host star, Gliese 12 b is unlikely to have retained a primordial or secondary atmosphere rich in H_2/He (see Section 7.3). None the less, owing to the brightness of its host star, Gliese 12 b stands as one of the top rocky targets for atmospheric follow-up with *JWST*. Following E. M. R. Kempton et al. (2018), we used the planetary mass and radius, stellar radius, equilibrium temperature, and the apparent stellar magnitude in the *J* band to calculate a Transmission Spectroscopy Metric of 14^{+7}_{-4}, similar to that of TRAPPIST-1 e, f, g, and h.

We conducted simulations of transmission and emission spectra for realistic atmospheric scenarios, as they would be observed with various *JWST* instrument configurations (Fig. 11). In particular, we modelled a Venus-like atmosphere consisting of 100 per cent CO_2, motivated by the planet's physical parameters resembling those of Venus (see Section 7.1); a steam H_2O envelope representing a water-world scenario; and a lighter steam CH_4 envelope featuring a reduced environment. We used TAUREX3 for radiative transfer modelling (I. P. Waldmann et al. 2015a, b; A. F. Al-Refaie et al. 2021), employing a temperature–pressure profile similar to that of Venus for the CO_2 atmosphere and profiles adapted from E. M. R. Kempton et al. (2023) for the H_2O and CH_4 compositions. The absorption cross sections for H_2O, CO_2, and CH_4 were obtained from the ExoMol database (K. L. Chubb et al. 2021), which utilized line lists by O. L. Polyansky et al. (2018), L. S. Rothman et al. (2010), and S. N. Yurchenko et al. (2017), respectively. The corresponding *JWST* spectra were generated using EXOTETHYS (G. Morello et al. 2021) for the NIRSpec *G*140*H* (0.97–1.83 μm), *G*235*H* (1.66–3.07 μm),

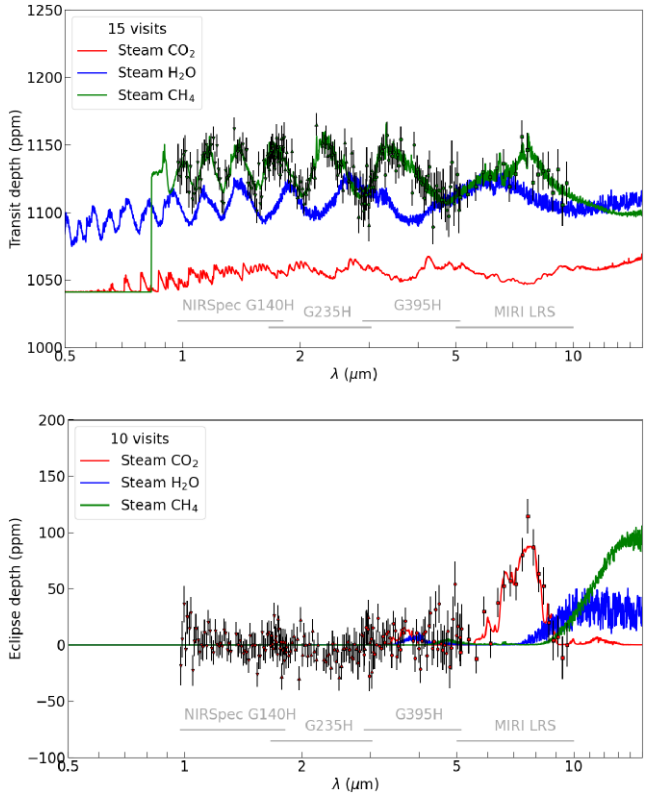

Figure 11. Top panel: modelled transmission spectra of Gliese 12 b, assuming an atmospheric composition of 100 per cent CO_2 (red), 100 per cent H_2O (blue), and 100 per cent CH_4 (green). Points with error bars show the simulated spectrum for the CH_4 composition, combining 15 transits with each of the NIRSpec *G*140*H*, *G*235*H*, *G*395*H*, and MIRI LRS slitless modes. Bottom panel: analogous emission spectra. Points with error bars show the simulated spectrum for the CO_2 composition, combining 10 eclipses with each of the NIRSpec *G*140*H*, *G*235*H*, *G*395*H*, and MIRI LRS slitless modes.

and *G*395*H* (2.88–5.18 μm) modes, as well as the Mid-Infrared Instrument (MIRI) LRS Slitless (5–10 μm) mode, based on updated instrument response files. We included an additional 30 per cent noise contribution in the final error bars. The popular Near-Infrared Imager and Slitless Spectrograph Single Object Slitless Spectroscopy (NIRISS SOSS) mode was excluded due to detector saturation after the first group. We adopted spectroscopic binning with a resolving power of $\mathcal{R} \sim 100$ for the NIRSpec modes, following the recommendations of A. L. Carter et al. (2024) and J. J. Davey et al. (2025), and a constant bin size of 0.25 μm for the MIRI LRS, as suggested by D. Powell et al. (2024). The predicted error bars for a single transit observation are 32–54 ppm (mean error 37 ppm) for NIRSpec *G*140*H*, 32–52 ppm (mean error 38 ppm) for NIRSpec *G*235*H*, 36–68 ppm (mean error 46 ppm) for NIRSpec *G*395*H*, and 40–61 ppm (mean error 48 ppm) for MIRI LRS. These uncertainties are comparable to or smaller than the expected spectral features in transmission, which reach $\lesssim$50 ppm in the most favourable CH_4-dominated scenario. The emission spectra are generally flat across the wavelength range covered by our instrumental simulations, except for a ∼90 ppm CO_2 feature in the Venus-like scenario.

Another possibility is to measure planetary emission at longer wavelengths. In fact, Gliese 12 b is a target under consideration for the Rocky World DDT program (S. Redfield et al. 2024), potentially aiming to observe multiple secondary eclipses using a MIRI filter centred at 15 μm. In all cases, multiple visits are required to robustly detect atmospheric features, with the optimal strategy, transmission or emission spectroscopy, depending on the actual atmospheric composition of Gliese 12 b.

7.5 Possibility of extra planets in the system

The possibility of there being more planets within the system still remains, and further investigation is needed to reveal any previously undetected signals. We have performed additional RV fits using two eccentric Keplerian models to explore any potential multiplanet configurations of small planets with periods below 50 d (based of the periodogram information). While a solution was found with a second Keplerian close to 34 d, the parameters were poorly constrained and the single-Keplerian model with a GP applied to the RVs was preferred using the BIC. We obtained BIC = −1774.7 versus BIC = −1846.5 for the two-Keplerian model and the adopted model, respectively.

Ultimately, more data are required to constrain any existing secondary signals, and authenticate the system architecture. More RV data will further allow for the resolution of current degeneracies that exist between eccentricity, stellar activity, and any undetected planetary companions and make the mass measurement of Gliese 12 b more robust. Obtaining more RVs with the precision of those within this study could reveal planets hidden below the current precision floor of the data set.

8 CONCLUSIONS

In this paper, we present new analyses of the transiting exo-Venus, Gliese 12 b. We performed a photometry-only fit with JULIET, an informed RV fit with PYANETI, and a joint fit using both data sets simultaneously with PYORBIT. All orbital and planetary parameters are consistent across fits and modelling software.

With new *TESS* and *CHEOPS* observations, we report refined orbital period (12.76 d) and planetary radius measurements ($0.93 \pm 0.06\,R_\oplus$). Our updated radius value is consistent with the values reported in previous studies (S. Dholakia et al. 2024; M. Kuzuhara et al. 2024).

Using nearly 200 high-precision RV observations from HARPS-N, ESPRESSO, and CARMENES, we report the first definitive mass measurement of Gliese 12 b. Owing to the extremely small RV semi-amplitude of Gliese 12 b, we adopted a variety of modelling approaches dealing with the stellar signals in different ways. We detect an RV semi-amplitude of $0.67 \pm 0.21\,m\,s^{-1}$ (3.2σ), yielding a mass measurement of $0.95^{+0.29}_{-0.30}\,M_\oplus$. This measurement is among the smallest semi-amplitudes ever measured for a transiting planet and is pushing the boundaries of our current capabilities.

A thorough investigation was conducted into the activity signal of Gliese 12. Analysis of long-term photometric monitoring from ASAS-SN, LCOGT, TJO, and E-EYE – as well as a DCF analysis of the RV and Hα data – provided further evidence towards a stellar rotation period of approximately 85 d (see Fig. A1). This work highlights the importance of the rigorous treatment of stellar variability when searching for the smallest exoplanets in RV data.

Gliese 12 b stands out with its physical and orbital properties. We investigated the nature of Gliese 12 b, by studying its interior structure, atmospheric mass-loss history, and future atmospheric prospects. Interior structure modelling revealed that Gliese 12 b is likely to be similar to Venus in composition (predominantly rocky make-up). The bulk properties of this planet place it in a unique region of parameter space, distinguishing it from other exoplanets with similar properties (see Figs 6 and 7). Furthermore, we demonstrated

that the planet is unlikely to have retained a primordial gaseous envelope, due to the X-ray emission history of its host star. Given its intriguing properties, Gliese 12 b presents a promising opportunity for Lyman-α spectroscopic follow-up studies, and is already being observed with *HST* for this reason. It is also a fantastic target for the Rocky Worlds DDT programme on *JWST*.

ACKNOWLEDGEMENTS

We thank the referee for a constructive and timely report that improved the quality of this manuscript.

This work is based on observations made with the Italian Telescopio Nazionale Galileo (TNG) operated on the island of La Palma by the Fundación Galileo Galilei of the INAF (Istituto Nazionale di Astrofisica) at the Spanish Observatorio del Roque de los Muchachos of the Instituto de Astrofisica de Canarias. The HARPS-N project was funded by the Prodex Program of the Swiss Space Office (SSO), the Harvard University Origin of Life Initiative (HUOLI), the Scottish Universities Physics Alliance (SUPA), the University of Geneva, the Smithsonian Astrophysical Observatory (SAO), the Italian National Astrophysical Institute (INAF), University of St. Andrews, Queen's University Belfast, and University of Edinburgh.

CARMENES is an instrument at the Centro Astronómico Hispano en Andalucía (CAHA) at Calar Alto (Almería, Spain), operated jointly by the Junta de Andalucía and the Instituto de Astrofísica de Andalucía (CSIC). CARMENES was funded by the Max-Planck-Gesellschaft (MPG), the Consejo Superior de Investigaciones Científicas (CSIC), the Ministerio de Economía y Competitividad (MINECO), and the European Regional Development Fund (ERDF) through projects FICTS-2011-02, ICTS-2017-07-CAHA-4, and CAHA16-CE-3978, and the members of the CARMENES Consortium (Max-Planck-Institut für Astronomie, Instituto de Astrofísica de Andalucía, Landessternwarte Königstuhl, Institut de Ciències de l'Espai, Institut für Astrophysik Göttingen, Universidad Complutense de Madrid, Thüringer Landessternwarte Tautenburg, Instituto de Astrofísica de Canarias, Hamburger Sternwarte, Centro de Astrobiología and Centro Astronómico Hispano-Alemán), with additional contributions by the MINECO, the Deutsche Forschungsgemeinschaft (DFG) through the Major Research Instrumentation Programme and Research Unit FOR2544 'Blue Planets around Red Stars', the Klaus Tschira Stiftung, the states of Baden-Württemberg and Niedersachsen, and by the Junta de Andalucía.

This work is based on observations collected with ESPRESSO at the European Southern Observatory under ESO programme 113.26RH.

CHEOPS is an ESA mission in partnership with Switzerland with important contributions to the payload and the ground segment from Austria, Belgium, France, Germany, Hungary, Italy, Portugal, Spain, Sweden, and the United Kingdom. The *CHEOPS* Consortium would like to gratefully acknowledge the support received by all the agencies, offices, universities, and industries involved. Their flexibility and willingness to explore new approaches were essential to the success of this mission. *CHEOPS* data analysed in this article will be made available in the *CHEOPS* mission archive (https://cheops.unige.ch/archive_browser/).

This paper made use of data collected by the *TESS* mission and are publicly available from the Mikulski Archive for Space Telescopes (MAST) operated by the Space Telescope Science Institute (STScI). Funding for the *TESS* mission is provided by NASA's Science Mission Directorate. We acknowledge the use of public *TESS* data from pipelines at the *TESS* Science Office and at the *TESS* Science Processing Operations Center. Resources supporting this work were provided by the NASA High-End Computing (HEC) Program through the NASA Advanced Supercomputing (NAS) Division at Ames Research Center for the production of the SPOC data products. This research has made use of the Exoplanet Follow-up Observation Programme (ExoFOP; doi:10.26134/ExoFOP5) website, which is operated by the California Institute of Technology, under contract with the National Aeronautics and Space Administration under the Exoplanet Exploration Programme.

This article is based on observations made with the MuSCAT2 instrument, developed by ABC, at Telescopio Carlos Sánchez, operated on the island of Tenerife by the IAC in the Spanish Observatorio del Teide.

This paper is based on observations made with the MuSCAT3 instrument, developed by the Astrobiology Center and under financial supports by JSPS KAKENHI (JP18H05439) and JST PRESTO (JPMJPR1775), at Faulkes Telescope North on Maui, HI, operated by the Las Cumbres Observatory.

This work has made use of data from the European Space Agency (ESA) mission *Gaia* (https://www.cosmos.esa.int/gaia), processed by the *Gaia* Data Processing and Analysis Consortium (DPAC, https://www.cosmos.esa.int/web/gaia/dpac/consortium). Funding for the DPAC has been provided by national institutions, in particular the institutions participating in the *Gaia* Multilateral Agreement.

This publication makes use of The Data & Analysis Center for Exoplanets (DACE), which is a facility based at the University of Geneva (CH) dedicated to extrasolar planets data visualization, exchange, and analysis. DACE is a platform of the Swiss National Centre of Competence in Research (NCCR) PlanetS, federating the Swiss expertise in Exoplanet research. The DACE platform is available at https://dace.unige.ch.

This research has made use of the NASA Exoplanet Archive, which is operated by the California Institute of Technology, under contract with the National Aeronautics and Space Administration under the Exoplanet Exploration Program.

DAT acknowledges the support of the Science and Technology Facilities Council (STFC).

YNEE acknowledges support from a Science and Technology Facilities Council (STFC) studentship, grant no. ST/Y509693/1.

AM, AAJ, and BSL acknowledge funding from a UKRI Future Leader Fellowship, grant no. MR/X033244/1. AM acknowledges funding from a UK Science and Technology Facilities Council (STFC) small grant ST/Y002334/1.

TGW acknowledges support from the University of Warwick and UKSA.

We acknowledge financial support from the Agencia Estatal de Investigación of the Ministerio de Ciencia e Innovación MCIN/AEI/10.13039/501100011033, the ERDF 'A way of making Europe', and the Fondo Social Europeo plus (FSE+) through projects PID2023-152906NA-I00, PID2022-137241NBC4[1:4], PID2021-125627OB-C3[1:2], PID2020-112949GB-I00, PID2019-107061GB-C61, CNS2023-144309, and RYC2022-037854-I, and from the Centre of Excellence 'Severo Ochoa' award to the Instituto de Astrofisica de Canarias (CEX2021-001131-S).

This research was partially funded by The Israel Science Foundation through grant no. 1404/22.

This work was funded by the European Union (ERC, FIERCE, 101052347). Views and opinions expressed are however those of the author(s) only and do not necessarily reflect those of the European Union or the European Research Council. Neither the European Union nor the granting authority can be held responsible for them. This work was also supported by FCT–

Fundação para a Ciência e a Tecnologia through national funds by these grants: UIDB/04434/2020, doi:10.54499/UIDB/04434/2020, UIDP/04434/2020, doi:10.54499/UIDP/04434/2020, PTDC/FIS-AST/4862/2020, UID/04434/2025. CEECIND/CP2839/CT0004, 2023.08117.CEECIND/CP2839/CT0004.

SD and APH acknowledge support from the DFG under Research Unit FOR2544 'Blue Planets around Red Stars' through projects DR 281/39-1 and HA 3279/14-1, respectively.

LN and LM acknowledge financial contribution from the INAF Large Grant 2023 'EXODEMO'.

AVF acknowledges the support of the Institude of Physics through the Bell Burnell Graduate Scholarship Fund.

LM acknowledges the financial contribution from PRIN MUR 2022 project 2022J4H55R.

ASB acknowledges financial contribution from the European Union–Next Generation EU RRF M4C2 1.1 PRIN MUR 2022 project 2022CERJ49 (ESPLORA).

TT acknowledges support from the BNSF program 'VIHREN-2021' project no. KP-06-DV/5.

IC acknowledges financial contribution from the European Union–Next Generation EU PNRR M4C2 1.2 project SOE2024.

MS thanks the Belgian Federal Science Policy Office (BELSPO) for the provision of financial support in the framework of the PRODEX Programme of the European Space Agency (ESA) under contract no. C4000140754.

This work has been carried out within the framework of the NCCR PlanetS supported by the Swiss National Science Foundation under grants 51NF40_182901 and 51NF40_205606.

ACC acknowledges support from STFC consolidated grant no. ST/V000861/1 and UKRI/ERC Synergy Grant EP/Z000181/1 (REVEAL).

EN acknowledges the support from the Deutsches Zentrum für Luft- und Raumfahrt (DLR, German Aerospace Center) – project no. 50OP2502.

DATA AVAILABILITY

The photometric data are publicly available via the respective archives. The RVs will be released via Vizier CDS. Further corner plots and posterior distributions are available upon request.

REFERENCES

Adibekyan V. et al., 2021, Science, 374, 330
Agol E. et al., 2021, Planet. Sci. J., 2, 1
Al-Refaie A. F., Changeat Q., Waldmann I. P., Tinetti G., 2021, ApJ, 917, 37
Alvarez R., Plez B., 1998, A&A, 330, 1109
Asplund M., Grevesse N., Sauval A. J., Scott P., 2009, ARA&A, 47, 481
Astudillo-Defru N., Delfosse X., Bonfils X., Forveille T., Lovis C., Rameau J., 2017, A&A, 600, A13
Atri D., Mogan S. R. C., 2021, MNRAS, 500, L1
Baglin A., 2003, Adv. Space Res., 31, 345
Bailer-Jones C. A. L., Rybizki J., Fouesneau M., Demleitner M., Andrae R., 2021, AJ, 161, 147
Barragán O., Aigrain S., Rajpaul V. M., Zicher N., 2022, MNRAS, 509, 866
Barragán O., Gandolfi D., Antoniciello G., 2019, MNRAS, 482, 1017
Basant R. et al., 2025, ApJ, 982, L1
Batalha N. E., Lewis T., Fortney J. J., Batalha N. M., Kempton E., Lewis N. K., Line M. R., 2019, ApJ, 885, L25
Bauer F. F., Zechmeister M., Reiners A., 2015, A&A, 581, A117
Benz W. et al., 2021, Exp. Astron., 51, 109
Blanco-Cuaresma S., 2019, MNRAS, 486, 2075
Blanco-Cuaresma S., Soubiran C., Heiter U., Jofré P., 2014, A&A, 569, A111
Bonomo A. S. et al., 2023, A&A, 677, A33
Borucki W. J. et al., 2010, Science, 327, 977
Brandeker A., Patel J. A., Morris B. M., 2024, Astrophysics Source Code Library, record ascl:2404.002
Brown T. M. et al., 2013, PASP, 125, 1031
Caballero J. A. et al., 2016, in Peck A. B., Seaman R. L., Benn C. R. eds, Proc. SPIE Conf. Ser. Vol. 9910, Observatory Operations: Strategies, Processes, and Systems VI, p. 99100E
Cadieux C. et al., 2024, ApJ, 960, L3
Carter A. L. et al., 2024, Nat. Astron., 8, 1008
Chen H., Rogers L. A., 2016, ApJ, 831, 180
Christiansen J. L. et al., 2025. The Planetary Science Journal, 6, 186
Chubb K. L. et al., 2021, A&A, 646, A21
Cifuentes C. et al., 2020, A&A, 642, A115
Collier Cameron A. et al., 2019, MNRAS, 487, 1082
Collins K. A., Kielkopf J. F., Stassun K. G., Hessman F. V., 2017, AJ, 153, 77
Colomé J., Casteels K., Ribas I., Francisco X., 2010, in Radziwill N. M., Bridger A. eds, Proc. SPIE Conf. Ser. vol. 7740, Software and Cyberinfrastructure for Astronomy, p. 77403K
Colome J., Ribas I., 2006, IAU Special Session, 6, 11
Cortés-Contreras M. et al., 2024, A&A, 692, A206
Cosentino R. et al., 2012, in McLean I. S., Ramsay S. K., Takami H. eds, Proc. SPIE Conf. Ser. Vol. 8446, Ground-based and Airborne Instrumentation for Astronomy IV, p. 84461V
Cowan N. B., Agol E., 2011, ApJ, 729, 54
Davey J. J., Yip K. H., Al-Refaie A. F., Waldmann I. P., 2025, MNRAS, 536, 2618
Demangeon O. D. S. et al., 2021, A&A, 653, A41
Dholakia S. et al., 2024, MNRAS, 531, 1276
Dressing C. D., Charbonneau D., 2015, ApJ, 807, 45
Dumusque X. et al., 2021, A&A, 648, A103
Eastman J., Gaudi B. S., Agol E., 2013, PASP, 125, 83
Edelson R. A., Krolik J. H., 1988, ApJ, 333, 646
Egger J. A. et al., 2024, A&A, 688, A223
Ehrenreich D. et al., 2015, Nature, 522, 459
Engle S. G., 2024, ApJ, 960, 62
Engle S. G., Guinan E. F., 2023, ApJ, 954, L50
Espinoza N., Kossakowski D., Brahm R., 2019, MNRAS, 490, 2262
Fernández Fernández J., Wheatley P. J., King G. W., 2023, MNRAS, 522, 4251
Foreman-Mackey D., Agol E., Ambikasaran S., Angus R., 2017, AJ, 154, 220
Foreman-Mackey D., Hogg D. W., Lang D., Goodman J., 2013, PASP, 125, 306
Gaia Collaboration, 2023, A&A, 674, A1
Gibson N. P., Aigrain S., Roberts S., Evans T. M., Osborne M., Pont F., 2012, MNRAS, 419, 2683
Gillon M. et al., 2017, Nature, 542, 456
Gromek N., 2025, Master's thesis, McMaster University, Canada
Gustafsson B., Edvardsson B., Eriksson K., Jørgensen U. G., Nordlund Å., Plez B., 2008, A&A, 486, 951
Haldemann J., Dorn C., Venturini J., Alibert Y., Benz W., 2024, A&A, 681, A96
Hazra G., Vidotto A. A., Carolan S., Villarreal D'Angelo C., Ó Fionnagáin D., 2025, MNRAS, 536, 1089
Hejazi N., Crossfield I. J. M., Nordlander T., Souto D., Masseron T., Marfil E., 2023, in American Astronomical Society Meeting Abstracts #241, p. 415.02
Hinkel N. R., Young P. A., Wheeler C. H. III, 2022, AJ, 164, 256
Hoyer S., Guterman P., Demangeon O., Sousa S. G., Deleuil M., Meunier J. C., Benz W., 2020, A&A, 635, A24
Husser T. O., Wende-von Berg S., Dreizler S., Homeier D., Reiners A., Barman T., Hauschildt P. H., 2013, A&A, 553, A6
Johnstone C. P., Bartel M., Güdel M., 2021, A&A, 649, A96
Kempton E. M. R. et al., 2018, PASP, 130, 114401

Kempton E. M. R., Lessard M., Malik M., Rogers L. A., Futrowsky K. E., Ih J., Marounina N., Romero-Mirza C. E., 2023, ApJ, 953, 57
King G. W. et al., 2018, MNRAS, 478, 1193
Kipping D. M., 2013, MNRAS, 435, 2152
Kochanek C. S. et al., 2017, PASP, 129, 104502
Kopparapu R. K., Ramirez R. M., SchottelKotte J., Kasting J. F., Domagal-Goldman S., Eymet V., 2014, ApJ, 787, L29
Kreidberg L., 2015, PASP, 127, 1161
Kubyshkina D. et al., 2018, A&A, 619, A151
Kubyshkina D. I., Fossati L., 2021, Res. Notes Am. Astron. Soc., 5, 74
Kupka F., Dubernet M. L., VAMDC Collaboration, 2011, Balt. Astron., 20, 503
Kuzuhara M. et al., 2024, ApJ, 967, L21
Lafarga M. et al., 2020, A&A, 636, A36
Linsky J. L., France K., Ayres T., 2013, ApJ, 766, 69
Malavolta L. et al., 2016, A&A, 588, A118
Malavolta L. et al., 2018, AJ, 155, 107
Marfil E. et al., 2021, A&A, 656, A162
Maxted P. F. L. et al., 2022, MNRAS, 514, 77
McCully C., Volgenau N. H., Harbeck D.-R., Lister T. A., Saunders E. S., Turner M. L., Siiverd R. J., Bowman M., 2018, in Guzman J. C., Ibsen J., eds, Proc. SPIE, p. 107070K
Morello G., Zingales T., Martin-Lagarde M., Gastaud R., Lagage P.-O., 2021, AJ, 161, 174
Mortier A. et al., 2020, MNRAS, 499, 5004
Mortier A., 2022, in The 21st Cambridge Workshop on Cool Stars, Stellar Systems, and the Sun, p. 71
Mortier A., Faria J. P., Correia C. M., Santerne A., Santos N. C., 2015, A&A, 573, A101
Murgas F. et al., 2023, A&A, 677, A182
Nagel E. et al., 2023, A&A, 680, A73
Narita N. et al., 2019, J. Astron. Telesc. Instrum. Syst., 5, 015001
Narita N. et al., 2020, in Evans C. J., Bryant J. J., Motohara K. eds, Proc. SPIE Conf. Ser. Vol. 11447, Ground-based and Airborne Instrumentation for Astronomy VIII, p. 114475K
Newton E. R., Charbonneau D., Irwin J., Berta-Thompson Z. K., Rojas-Ayala B., Covey K., Lloyd J. P., 2014, AJ, 147, 20
Newton E. R., Irwin J., Charbonneau D., Berta-Thompson Z. K., Dittmann J. A., West A. A., 2016, ApJ, 821, 93
Owen J. E., Jackson A. P., 2012, MNRAS, 425, 2931
Parc L., Bouchy F., Venturini J., Dorn C., Helled R., 2024, A&A, 688, A59
Parviainen H., 2015, MNRAS, 450, 3233
Parviainen H., Aigrain S., 2015, MNRAS, 453, 3821
Paxton B., Bildsten L., Dotter A., Herwig F., Lesaffre P., Timmes F., 2011, ApJS, 192, 3
Pepe F. et al., 2011, A&A, 534, A58
Pepe F. et al., 2014, Astron. Nachr., 335, 8
Pepe F. et al., 2021, A&A, 645, A96
Perger M., Anglada-Escudé G., Ribas I., Rosich A., Herrero E., Morales J. C., 2021, A&A, 645, A58
Plez B., 2012, Astrophysics Source Code Library, record ascl:1205.004
Polyansky O. L., Kyuberis A. A., Zobov N. F., Tennyson J., Yurchenko S. N., Lodi L., 2018, MNRAS, 480, 2597
Powell D. et al., 2024, Nature, 626, 979
Queloz D. et al., 2001, A&A, 379, 279
Quirrenbach A. et al., 2014, in Ramsay S. K., McLean I. S., Takami H., eds, Ground-based and Airborne Instrumentation for Astronomy V, p. 91471F
Quirrenbach A. et al., 2018, in Evans C.J., Simard L., Takami H., eds, Ground-based and Airborne Instrumentation for Astronomy VII, p. 107020W
Rajpaul V., Aigrain S., Osborne M. A., Reece S., Roberts S., 2015, MNRAS, 452, 2269
Rasmussen C., Williams C., 2010, in Dietterich T., Bishop C., Heckerman D., Jordan M., Kearns M., eds, Gaussian Processes for Machine Learning. The MIT Press, Cambridge, MA, p. 935
Redfield S. et al., 2024, preprint (arXiv:2404.02932)
Redfield S., Linsky J. L., 2000, ApJ, 534, 825
Reiners A. et al., 2018, A&A, 612, A49
Ricker G. R. et al., 2015, J. Astron. Telesc. Instrum. Syst., 1, 014003
Ricker G., 2021, in 43rd COSPAR Scientific Assembly. Held 28 January–4 February, p. 499
Rogers J. G., Owen J. E., Schlichting H. E., 2024, MNRAS, 529, 2716
Rothman L. S. et al., 2010, J. Quant. Spec. Radiat. Transf., 111, 2139
Sabotta S. et al., 2021, A&A, 653, A114
Sanz-Forcada J. et al., 2025, A&A, 693, A285
Schweitzer A. et al., 2019, A&A, 625, A68
Shan Y. et al., 2024, A&A, 684, A9
Shappee B. J. et al., 2014, ApJ, 788, 48
Shields A. L., Ballard S., Johnson J. A., 2016, Phys. Rep., 663, 1
Silva A. M. et al., 2022, A&A, 663, A143
Souto D. et al., 2017, ApJ, 835, 239
Stalport M. et al., 2025, A&A, 696, A86
Tabernero H. M., Marfil E., Montes D., González Hernández J. I., 2022, A&A, 657, A66
Tal-Or L. et al., 2018, A&A, 614, A122
Thiabaud A., Marboeuf U., Alibert Y., Leya I., Mezger K., 2015, A&A, 580, A30
Trifonov T. et al., 2018, A&A, 609, A117
Vidal-Madjar A., Lecavelier des Etangs A., Désert J. M., Ballester G. E., Ferlet R., Hébrard G., Mayor M., 2003, Nature, 422, 143
Vidotto A. A., Jardine M., Morin J., Donati J. F., Lang P., Russell A. J. B., 2013, A&A, 557, A67
Waldmann I. P., Rocchetto M., Tinetti G., Barton E. J., Yurchenko S. N., Tennyson J., 2015b, ApJ, 813, 13
Waldmann I. P., Tinetti G., Rocchetto M., Barton E. J., Yurchenko S. N., Tennyson J., 2015a, ApJ, 802, 107
Webb N. A. et al., 2020, A&A, 641, A136
Wilson T. G. et al., 2022, MNRAS, 511, 1043
Yurchenko S. N., Amundsen D. S., Tennyson J., Waldmann I. P., 2017, A&A, 605, A95
Zechmeister M. et al., 2018, A&A, 609, A12
Zechmeister M., Anglada-Escudé G., Reiners A., 2014, A&A, 561, A59
Zechmeister M., Kürster M., 2009, A&A, 496, 577
Zeng L. et al., 2019, Proc. Natl. Acad. Sci., 116, 9723

APPENDIX A: LONG-TERM PHOTOMETRY

Fig. A1 shows the long-term photometry used in Section 3.2 to determine the stellar rotation period.

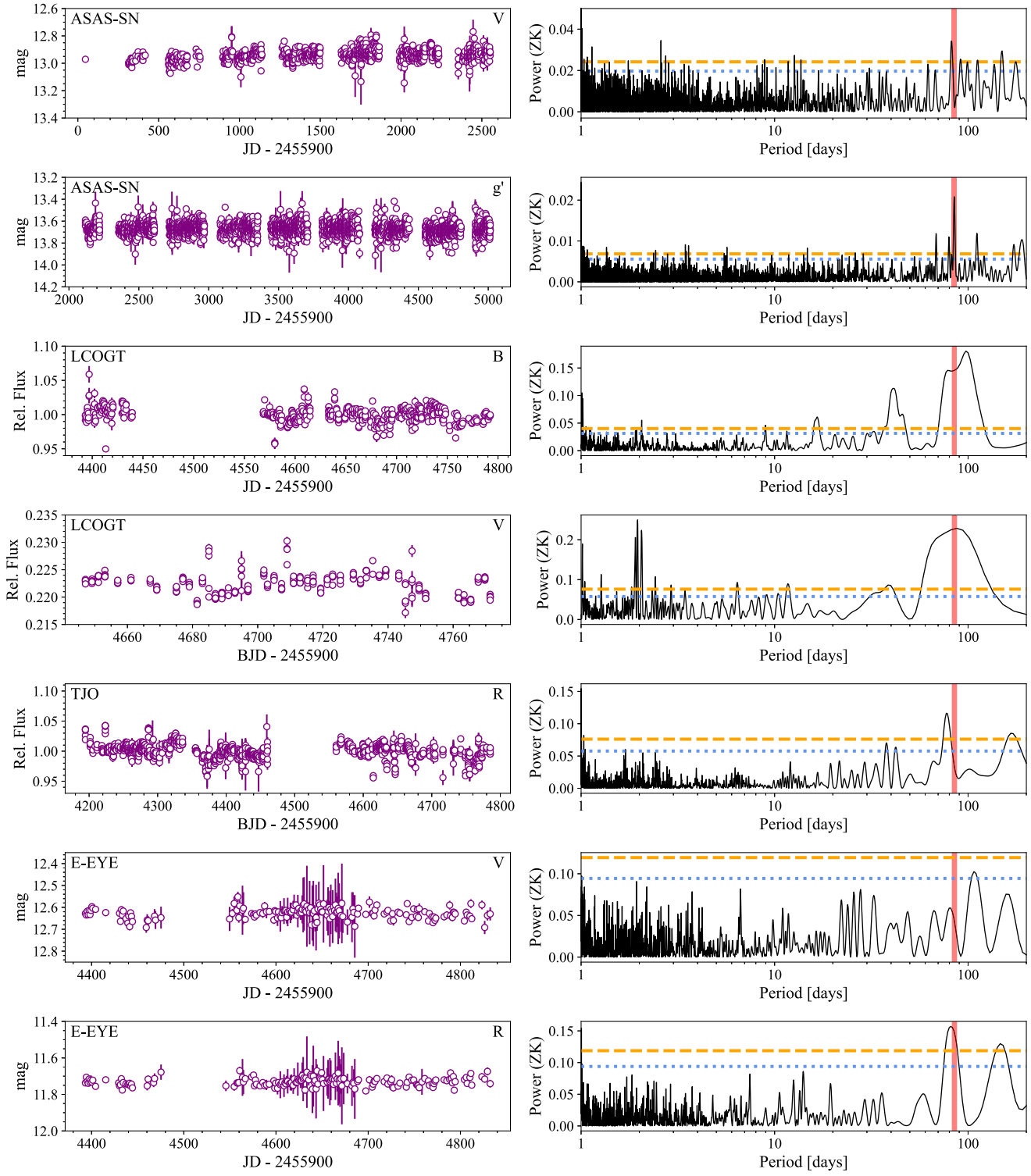

Figure A1. Gliese 12 long-term ground-based photometry and GLS periodograms of the time-series. The vertical red line marks the rotation period $P_{\rm rot} = 85$ d presented by M. Kuzuhara et al. (2024), and the horizontal lines represent the 10 per cent (blue dotted) and 1 per cent (orange dashed) false alarm probability levels.

APPENDIX B: RV PERIODOGRAMS AND DATA

Fig. B1 shows the periodograms for the RV and Hα time-series for HARPS-N, ESPRESSO, and CARMENES. Table B1 contains a small sample of the RV data used in both the informed RV fit and the joint fit.

Table B1. A sample of the RV data used in the informed RV fit and the joint fit. The full table is available on Vizier.

BJD (d)	RV ($m\,s^{-1}$)	σ_{RV} ($m\,s^{-1}$)	Hα	$\sigma_{H\alpha}$	Instrument
2560165.657371	51335.99	1.42	−0.00392	0.00044	HARPS-N
2560171.600859	51336.51	1.69	0.02884	0.00069	HARPS-N
2560172.701740	51330.45	1.39	−0.00319	0.00052	HARPS-N
2560173.618065	51334.65	1.26	0.01949	0.00057	HARPS-N
2560174.667788	51332.18	1.28	0.00530	0.00056	HARPS-N
...	...	...	...	...	...
2560467.902064	51413.63	0.30	−0.00608	0.00014	ESPRESSO
2560473.887225	51410.06	0.33	−0.00361	0.00017	ESPRESSO
2560478.903217	51409.70	0.46	−0.01765	0.00026	ESPRESSO
2560479.905718	51408.93	0.29	−0.00962	0.00015	ESPRESSO
2560486.883796	51409.36	0.50	0.02229	0.00030	ESPRESSO
...	...	...	...	...	...
2560123.593106	−0.27	2.01	0.00678	0.00331	CARMENES
2560124.593296	1.74	2.83	0.01442	0.00443	CARMENES
2560125.643064	−0.69	1.41	−0.00233	0.00222	CARMENES
2560127.644050	−0.52	1.68	0.01458	0.00207	CARMENES
2560133.611007	−1.22	2.61	0.00517	0.00304	CARMENES
...	...	...	...	...	...

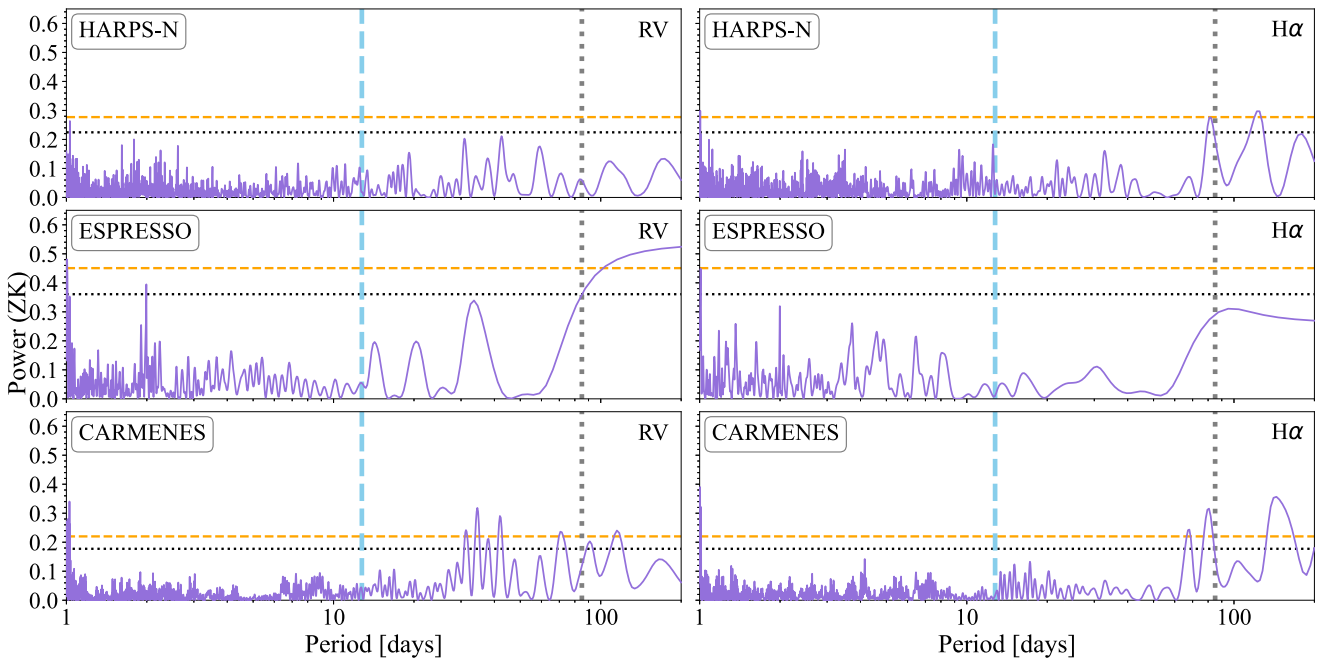

Figure B1. GLS periodograms for the RV and Hα data from all three instruments. The vertical lines in the plot are the orbital period of Gliese 12 b (light blue dashed line, $P = 12.7614$ d), and $P_{rot} = 85$ d (grey dotted line). The horizontal lines are the false alarm probabilities (FAP) = 10 per cent (black dotted line) and 1 per cent (orange dashed line).

APPENDIX C: PRIORS AND FITTED PARAMETERS

Tables C1 and C2 show the prior distributions used during the different fitting procedures. Table C3 has the final fitted values related to the star as well as the various instruments. The results of the joint fit are presented in Fig. C1, which shows the posteriors of the fitted parameters in a corner plot.

Table C1. Priors for the planetary parameters.

Parameter	Unit	Photometry-only fit	Informed RV fit	Joint fit
P	(d)	$\mathcal{N}(12.761408, 0.1)$	$\mathcal{N}(12.761422, 0.000047)$	$\mathcal{U}(12.46, 13.06)$
T_0	(BJD)	$\mathcal{N}(2459497.1865, 0.1)$	$\mathcal{N}(2460492.5747, 0.0044)$	$\mathcal{U}(2460032.86, 2460033.46)$
$R_p/R_\star$	–	$\mathcal{U}(0, 1)$	–	$\mathcal{U}(0.0, 0.5)$
b	–	$\mathcal{U}(0, 1)$	–	$\mathcal{U}(0, 1)$
$\rho_\star$	(g cm^{-3})	$\mathcal{N}(18.9879198, 15.950938)$	–	$\mathcal{N}(19.317, 1.409)$
K	(m s^{-1})	–	$\mathcal{U}(0, 2.5)$	$\mathcal{U}(0, 50)$
$\sqrt{e}\sin\omega$	–	–	$\mathcal{U}(-1, 1)$	$\mathcal{U}(-1, 1)$
$\sqrt{e}\cos\omega$	–	–	$\mathcal{U}(-1, 1)$	$\mathcal{U}(-1, 1)$
e	–	$\mathcal{U}(0, 0.9)$	–	$\mathcal{U}(0.0, 0.95)$
ω	(deg)	$\mathcal{U}(0, 360)$	–	$\mathcal{U}(0, 360)$

Table C2. Stellar and instrumental priors. We note that the coherence GP parameter is different for both fits due to a different functional form of the same kernel.

Parameter	Unit	Photometry-only fit	Informed RV fit	Joint fit
$P_{\rm rot,GP}$	(d)	–	$\mathcal{U}(25, 200)$	$\mathcal{U}(60, 200)$
Coherence	–	–	$\lambda_{\rm p} \in \mathcal{U}(0.01, 10)$	$w \in \mathcal{U}(0.001, 3.0)$
Evolution	(d)	–	$\lambda_{\rm e} \in \mathcal{U}(5, 1000)$	$\lambda \in \mathcal{U}(120.0, 1000.0)$
Amplitude	($\rm m\,s^{-1}$)	–	$A_0 \in \mathcal{U}(0, 10)$	$H, C \in \mathcal{U}(0, 50)$
Jitter HN	($\rm m\,s^{-1}$)	–	$\mathcal{U}(0, 100)$	$\mathcal{U}(0, 100)$
Jitter CARM	($\rm m\,s^{-1}$)	–	$\mathcal{U}(0, 100)$	$\mathcal{U}(0, 100)$
Jitter ESPR	($\rm m\,s^{-1}$)	–	$\mathcal{U}(0, 100)$	$\mathcal{U}(0, 100)$
Offset HN	($\rm m\,s^{-1}$)	–	$\mathcal{U}(51230.45, 51446.16)$	$\mathcal{U}(51000, 51800)$
Offset CARM	($\rm m\,s^{-1}$)	–	$\mathcal{U}(-106.67, 105.88)$	$\mathcal{U}(-50, 50)$
Offset ESPR	($\rm m\,s^{-1}$)	–	$\mathcal{U}(51305.26, 51513.63)$	$\mathcal{U}(51000, 51800)$
$\rm GP_\sigma$	(ppm)	$\mathcal{L}(0.000001, 1000000)$	–	$\log_{10}(\mathcal{U}(-6, 6))$
$\rm GP\rho$	(d)	$\mathcal{L}(0.001, 1000)$	–	$\log_{10}(\mathcal{U}(-3, 3))$
LD *TESS*		$q_1 \in \mathcal{U}(0, 1.0)$	–	$u_1 \in \mathcal{N}(0.26, 0.07)$
LD *TESS*		$q_2 \in \mathcal{U}(0, 1.0)$	–	$u_2 \in \mathcal{N}(0.29, 0.14)$
LD *CHEOPS*		$q_1 \in \mathcal{U}(0, 1.0)$	–	$u_1 \in \mathcal{N}(0.26, 0.04)$
LD *CHEOPS*		$q_2 \in \mathcal{U}(0, 1.0)$	–	$u_2 \in \mathcal{N}(0.28, 0.09)$
LD MuSCAT2 *r*		$q_1 \in \mathcal{U}(0, 1.0)$	–	–
LD MuSCAT2 *r*		$q_2 \in \mathcal{U}(0, 1.0)$	–	–
LD MuSCAT3 *r*		$q_1 \in \mathcal{U}(0, 1.0)$	–	–
LD MuSCAT3 *r*		$q_2 \in \mathcal{U}(0, 1.0)$	–	–
LD MuSCAT2 *i*		$q_1 \in \mathcal{U}(0, 1.0)$	–	–
LD MuSCAT2 *i*		$q_2 \in \mathcal{U}(0, 1.0)$	–	–
LD MuSCAT3 *i*		$q_1 \in \mathcal{U}(0, 1.0)$	–	–
LD MuSCAT3 *i*		$q_2 \in \mathcal{U}(0, 1.0)$	–	–
LD MuSCAT2 *z*		$q_1 \in \mathcal{U}(0, 1.0)$	–	–
LD MuSCAT2 *z*		$q_2 \in \mathcal{U}(0, 1.0)$	–	–
LD MuSCAT3 *z*		$q_1 \in \mathcal{U}(0, 1.0)$	–	–
LD MuSCAT3 *z*		$q_2 \in \mathcal{U}(0, 1.0)$	–	–
Offset *TESS*		$\mathcal{N}(0, 0.1)$	–	–
Offset *CHEOPS*		$\mathcal{N}(0, 0.1)$	–	–
Offset MuSCAT2 *r*		$\mathcal{N}(0, 0.1)$	–	–
Offset MuSCAT3 *r*		$\mathcal{N}(0, 0.1)$	–	–
Offset MuSCAT2 *i*		$\mathcal{N}(0, 0.1)$	–	–
Offset MuSCAT3 *i*		$\mathcal{N}(0, 0.1)$	–	–
Offset MuSCAT2 *z*		$\mathcal{N}(0, 0.1)$	–	–
Offset MuSCAT3 *z*		$\mathcal{N}(0, 0.1)$	–	–
Jitter *TESS*	(ppm)	$\mathcal{L}(0.1, 1000.0)$	–	$\mathcal{U}(0, 119800)$; $\mathcal{U}(0, 117600)$; $\mathcal{U}(0, 118000)$; $\mathcal{U}(0, 117600)$;
			–	$\mathcal{U}(0, 128000)$; $\mathcal{U}(0, 128500)$; $\mathcal{U}(0, 121600)$; $\mathcal{U}(0, 121100)$
Jitter *CHEOPS*	(ppm)	$\mathcal{L}(0.1, 100000.0)$	–	$\mathcal{U}(0, 69800)$; $\mathcal{U}(0, 62700)$; $\mathcal{U}(0, 67000)$; $\mathcal{U}(0, 63000)$;
			–	$\mathcal{U}(0, 62800)$; $\mathcal{U}(0, 251000)$
jitter MuSCAT2 *r*	(ppm)	$\mathcal{L}(0.1, 100000.0)$	–	–
Jitter MuSCAT3 *r*	(ppm)	$\mathcal{L}(0.1, 100000.0)$	–	–
Jitter MuSCAT2 *i*	(ppm)	$\mathcal{L}(0.1, 100000.0)$	–	–
Jitter MuSCAT3 *i*	(ppm)	$\mathcal{L}(0.1, 100000.0)$	–	–
Jitter MuSCAT2 *z*	(ppm)	$\mathcal{L}(0.1, 100000.0)$	–	–
Jitter MuSCAT3 *z*	(ppm)	$\mathcal{L}(0.1, 100000.0)$	–	–

Table C3. Stellar and instrumental parameters. We note that the coherence GP parameter is different for both fits due to a different functional form of the same kernel.

Parameter	Unit	Photometry-only fit	Informed RV fit	Joint fit
$P_{\rm rot,GP}$	(d)	–	$121.6^{+51.5}_{-61.8}$	$172.0^{+1.5}_{-1.6}$
Coherence	–	–	$\lambda_{\rm p} = 3.10^{+4.64}_{-2.87}$	$w = 0.212^{+0.054}_{-0.045}$
Evolution	(d)	–	$\lambda_{\rm e} = 9.61^{+56.53}_{-2.06}$	$\lambda = 476^{+267}_{-160}$
Amplitude	($\rm m\,s^{-1}$)	–	$A_0 = 2.04^{+0.44}_{-0.34}$	$H_{\rm HN} = 2.24^{+0.89}_{-0.65}$; $H_{\rm CARM} = 2.52^{+1.20}_{-0.75}$; $H_{\rm ESPR} = 0.84^{+0.18}_{-0.15}$
		–	–	$C_{\rm HN} = 0.78^{+1.10}_{-0.55}$; $C_{\rm CARM} = 1.07^{+1.60}_{-0.75}$; $C_{\rm ESPR} = 2.2^{+4.9}_{-1.6}$
Jitter HN	($\rm m\,s^{-1}$)	–	$1.37^{+0.32}_{-0.31}$	$1.70^{+0.34}_{-0.31}$
Jitter CARM	($\rm m\,s^{-1}$)	–	$0.25^{+0.29}_{-0.18}$	$0.35^{+0.35}_{-0.24}$
Jitter ESPR	($\rm m\,s^{-1}$)	–	$0.84^{+0.18}_{-0.14}$	$0.84^{+0.18}_{-0.15}$
Offset HN	($\rm m\,s^{-1}$)	–	51337.25 ± 0.56	$51337.18^{+0.96}_{-0.92}$
Offset CARM	($\rm m\,s^{-1}$)	–	$0.47^{+0.56}_{-0.54}$	$0.10^{+1.20}_{-1.00}$
Offset ESPR	($\rm m\,s^{-1}$)	–	$51409.56^{+0.59}_{-0.58}$	$51409.80^{+1.60}_{-1.30}$
GP$_\sigma$	(ppm)	$0.000192^{+0.000015}_{-0.000013}$	–	$\sigma_{\rm TESS} = 2.2^{+5.2}_{-1.0}$; $\sigma_{\rm TESS} = 2.1^{+4.9}_{-0.9}$; $\sigma_{\rm TESS} = 2.3^{+6.4}_{-1.1}$; $\sigma_{\rm TESS} = 2.0^{+3.8}_{-0.8}$
		–	–	$\sigma_{\rm TESS} = 2.3^{+5.7}_{-1.1}$; $\sigma_{\rm TESS} = 2.2^{+5.5}_{-1.0}$; $\sigma_{\rm TESS} = 2.0^{+4.0}_{-0.8}$; $\sigma_{\rm TESS} = 2.0^{+4.1}_{-0.8}$
		–	–	$\sigma_{\rm CHEOPS} = 3.0^{+11.2}_{-1.6}$; $\sigma_{\rm CHEOPS} = 3.3^{+20.1}_{-2.0}$; $\sigma_{\rm CHEOPS} = 2.6^{+8.1}_{-1.3}$
		–	–	$\sigma_{\rm CHEOPS} = 3.2^{+18.7}_{-1.8}$; $\sigma_{\rm CHEOPS} = 2.4^{+6.7}_{-1.1}$; $\sigma_{\rm CHEOPS} = 2.9^{+11.9}_{-1.6}$
GPρ	(d)	$0.621^{+0.075}_{-0.071}$	–	–
		–	–	$\rho_{\rm TESS} = 257.0^{+419.0}_{-205.8}$; $\rho_{\rm TESS} = 257.0^{+434.8}_{-202.1}$; $\rho_{\rm TESS} = 158.5^{+444.1}_{-131.6}$
		–	–	$\rho_{\rm TESS} = 331.1^{+410.2}_{-249.8}$ $\rho_{\rm TESS} = 208.9^{+436.7}_{-175.8}$; $\rho_{\rm TESS} = 204.2^{+441.5}_{-170.3}$
		–	–	$\rho_{\rm TESS} = 346.7^{+411.8}_{-257.6}$; $\rho_{\rm TESS} = 338.8^{+402.5}_{-251.7}$
		–	–	$\rho_{\rm CHEOPS} = 39.8^{+276.4}_{-35.0}$; $\rho_{\rm CHEOPS} = 4.1^{+14.1}_{-2.8}$; $\rho_{\rm CHEOPS} = 131.8^{+417.7}_{-116.3}$
		–	–	$\rho_{\rm CHEOPS} = 0.2^{+0.7}_{-0.1}$; $\rho_{\rm CHEOPS} = 154.9^{+447.7}_{-137.1}$; $\rho_{\rm CHEOPS} = 61.7^{+364.9}_{-57.8}$
LD *TESS*		$q_1 = 0.39^{+0.30}_{-0.23}$	–	$u_1 = 0.26^{+0.07}_{-0.07}$
LD *TESS*		$q_2 = 0.29^{+0.22}_{-0.18}$	–	$u_2 = 0.30^{+0.13}_{-0.13}$
LD *CHEOPS*		$q_1 = 0.18^{+0.19}_{-0.13}$	–	$u_1 = 0.26^{+0.04}_{-0.04}$
LD *CHEOPS*		$q_2 = 0.37^{+0.28}_{-0.22}$	–	$u_2 = 0.28^{+0.09}_{-0.09}$
LD MuSCAT2 *r*		$q_1 = 0.23^{+0.26}_{-0.16}$	–	–
LD MuSCAT2 *r*		$q_2 = 0.42^{+0.30}_{-0.27}$	–	–
LD MuSCAT3 *r*		$q_1 = 0.45^{+0.25}_{-0.22}$	–	–
LD MuSCAT3 *r*		$q_2 = 0.57^{+0.25}_{-0.26}$	–	–
LD MuSCAT2 *i*		$q_1 = 0.43^{+0.23}_{-0.24}$	–	–
LD MuSCAT2 *i*		$q_2 = 0.36^{+0.32}_{-0.24}$	–	–
LD MuSCAT3 *i*		$q_1 = 0.47^{+0.25}_{-0.24}$	–	–
LD MuSCAT3 *i*		$q_2 = 0.29^{+0.28}_{-0.20}$	–	–
LD MuSCAT2 *z*		$q_1 = 0.23^{+0.28}_{-0.16}$	–	–
LD MuSCAT2 *z*		$q_2 = 0.40^{+0.32}_{-0.26}$	–	–
LD MuSCAT3 *z*		$q_1 = 0.49^{+0.23}_{-0.23}$	–	–
LD MuSCAT3 *z*		$q_2 = 0.40^{+0.29}_{-0.25}$	–	–
Offset *TESS*		$0.000003^{+0.000021}_{-0.000021}$	–	–
Offset *CHEOPS*		$0.000163^{+0.000017}_{-0.000018}$	–	–
Offset MuSCAT2 *r*		$0.000419^{+0.000050}_{-0.000046}$	–	–
Offset MuSCAT3 *r*		$0.000017^{+0.000031}_{-0.000031}$	–	–
Offset MuSCAT2 *i*		$0.000022^{+0.000035}_{-0.000034}$	–	–
Offset MuSCAT3 *i*		$0.000032^{+0.000032}_{-0.000034}$	–	–
Offset MuSCAT2 *z*		$0.000050^{+0.000043}_{-0.000044}$	–	–
Offset MuSCAT3 *z*		$0.000012^{+0.000032}_{-0.000034}$	–	–

Table C3 – *continued*

Parameter	Unit	Photometry-only fit	Informed RV fit	Joint fit
Jitter *TESS*	(ppm)	$1.05^{+5.20}_{-0.81}$	–	114^{+100}_{-71}; 101^{+93}_{-63}; 390^{+110}_{-140}; 134^{+110}_{-85};
		–	–	160^{+130}_{-100}; 105^{+96}_{-65}; 99^{+90}_{-59}; 121^{+110}_{-76}
Jitter *CHEOPS*	(ppm)	$0.621^{+0.075}_{-0.071}$	–	380^{+49}_{-52}; 434^{+47}_{-49}; 356^{+75}_{-84}; 670^{+68}_{-66};
		–	–	204^{+96}_{-110}; 160^{+160}_{-100}
Jitter MuSCAT2 *r*	(ppm)	$784.91^{+51.39}_{-49.42}$	–	–
Jitter MuSCAT3 *r*	(ppm)	$599.73^{+46.93}_{-51.95}$	–	–
Jitter MuSCAT2 *i*	(ppm)	$1216.67^{+40.25}_{-39.34}$	–	–
Jitter MuSCAT3 *i*	(ppm)	$552.04^{+71.16}_{-84.80}$	–	–
Jitter MuSCAT2 *z*	(ppm)	$1335.90^{+48.65}_{-44.54}$	–	–
Jitter MuSCAT3 *z*	(ppm)	$405.06^{+156.39}_{-385.93}$	–	–

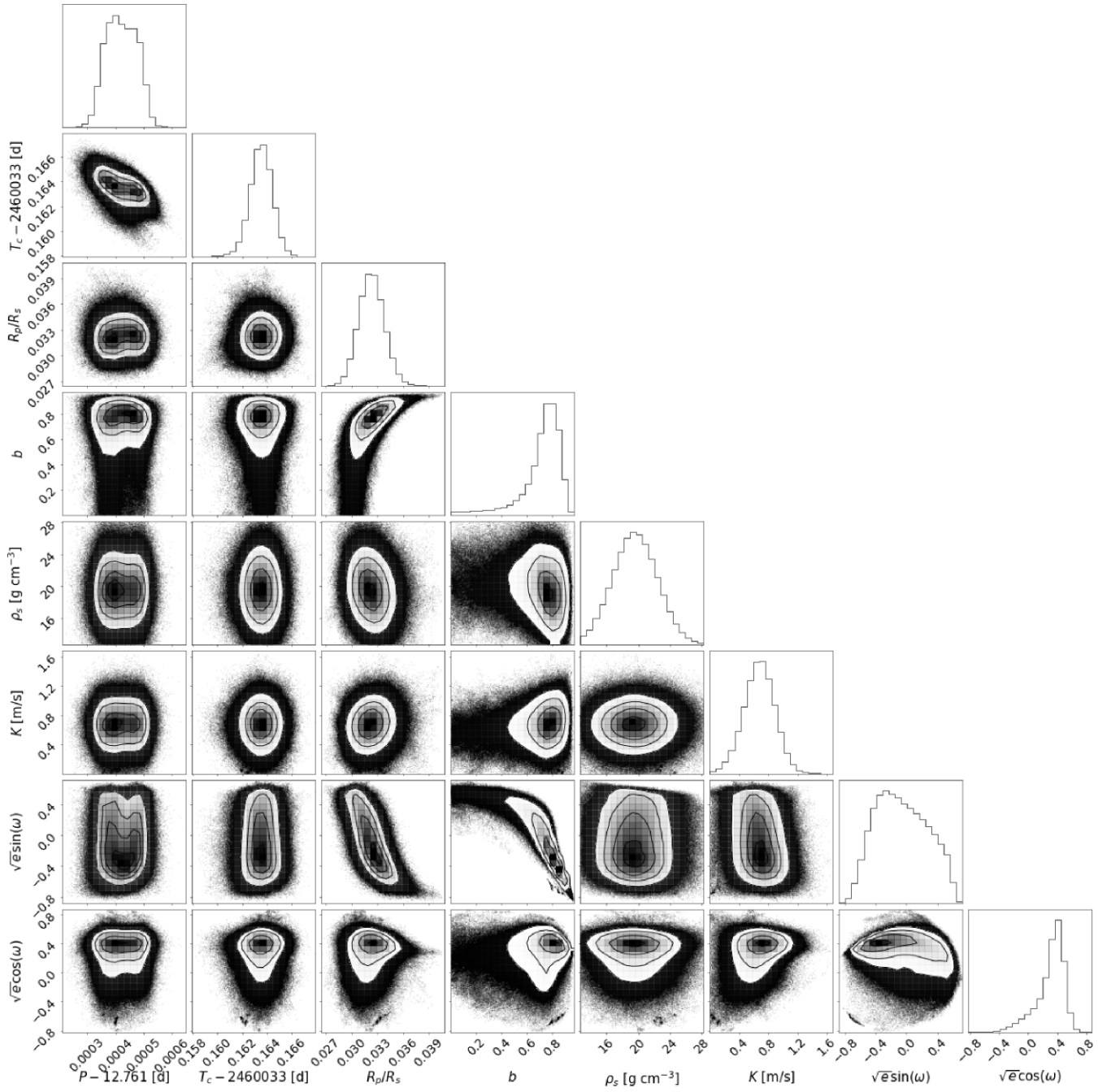

Figure C1. Corner plot for the fitted parameters of the joint fit.

[1]*School of Physics and Astronomy, University of Birmingham, Edgbaston, Birmingham B15 2TT, UK*
[2]*Department of Physics, University of Warwick, Gibbet Hill Road, Coventry CV4 7LS, UK*
[3]*Instituto de Astrofísica de Canarias (IAC), E-38205 La Laguna, Tenerife, Spain*
[4]*Departamento de Astrofísica, Universidad de La Laguna (ULL), E-38206 La Laguna, Tenerife, Spain*
[5]*Department of Physics & Astronomy, McMaster University, 1280 Main St W, Hamilton, ON L8S 4L8, Canada*
[6]*Instituto de Astrofísica de Andalucía (IAA), Glorieta de la Astronomía s/n, E-18080 Granada, Spain*
[7]*INAF – Osservatorio Astronomico di Palermo, Piazza del Parlamento, 1, I-90134 Palermo, Italy*
[8]*Institut de Ciències de l'Espai (ICE, CSIC), Campus UAB, c/ de Can Magrans s/n, 08193 Bellaterra, Spain*
[9]*Institut d'Estudis Espacials de Catalunya (IEEC), Edifici RDIT, Campus UPC, E-08860 Castelldefels (Barcelona), Spain*
[10]*Space Research and Planetary Sciences, Physics Institute, University of Bern, Gesellschaftsstrasse 6, CH-3012 Bern, Switzerland*
[11]*Carnegie Science Observatories, 813 Santa Barbara Street, Pasadena, CA 91101, USA*
[12]*Centro de Astrobiología (CSIC-INTA), Camino Bajo del Castillo s/n, 28692, Villanueva de la Cañada, Madrid, Spain*
[13]*Institut für Astrophysik und Geophysik, Georg-August-Universität, Friedrich-Hund-Platz 1, D-37077 Göttingen, Germany*
[14]*Thueringer Landessternwarte Tautenburg, Sternwarte 5, 07778, Tautenburg, Germany*
[15]*INAF – Osservatorio Astrofisico di Torino, Via Osservatorio 20, I-10025 Pino Torinese, Italy*
[16]*Vereniging Voor Sterrenkunde (VVS), Oostmeers 122 C, B-8000 Brugge, Belgium*
[17]*Public Observatory ASTROLAB IRIS, Provinciaal Domein 'De Palingbeek', Verbrandemolenstraat 5, B-8902 Zillebeke, Ieper, Belgium*
[18]*Centre for Astrophysics, University of Southern Queensland, Toowoomba, QLD 4350, Australia*
[19]*Department of Space Research and Space Technology, Technical University of Denmark, Elektrovej 328, DK-2800 Kgs. Lyngby, Denmark*
[20]*SUPA School of Physics and Astronomy, University of St Andrews, North Haugh, St Andrews KY16 9SS, UK*
[21]*Department of Astronomy and Astrophysics, Tata Institute of Fundamental Research, Mumbai, 400005, India*
[22]*Department of Physics, Ariel University, Ariel 40700, Israel*
[23]*Observatoire Astronomique de l'Université de Genève, Chemin Pegasi 51, CH-1290 Versoix, Switzerland*
[24]*Fundación Galileo Galilei – INAF, Rambla José Ana Fernandez Pérez 7, E-38712 Breña Baja, Tenerife, Spain*
[25]*Space Telescope Science Institute, 3700 San Martin Drive, Baltimore, MD 20218, USA*
[26]*Dipartimento di Fisica e Astronomia 'Galileo Galilei', Università di Padova, Vicolo dell'Osservatorio 3, I-35122 Padova, Italy*
[27]*Istituto Nazionale di Astrofisica – Osservatorio Astronomico di Padova, Vicolo dell'Osservatorio 5, I-35122 Padova, Italy*
[28]*Department of Physics, University of Rome 'Tor Vergata', Via della Ricerca Scientifica 1, I-00133 Roma, Italy*
[29]*Max Planck Institute for Astronomy, Königstuhl 17, 69117 Heidelberg, Germany*
[30]*Departamento de Física de la Tierra y Astrofísica and IPARCOS-UCM (Instituto de Física de Partículas y del Cosmos de la UCM), Facultad de Ciencias Físicas, Universidad Complutense de Madrid, E-28040 Madrid, Spain*
[31]*Department of Astronomy, University of Texas at Austin, 2515 Speedway, Austin, TX 78712, USA*
[32]*SUPA, Institute for Astronomy, University of Edinburgh, Blackford Hill, Edinburgh EH9 3HJ, UK*
[33]*Centre for Exoplanet Science, University of Edinburgh, Edinburgh EH9 3HJ, UK*
[34]*Landessternwarte, Zentrum für Astronomie der Universität Heidelberg, Königstuhl 12, D-69117 Heidelberg, Germany*
[35]*Instituto de Astrofísica e Ciências do Espaço, CAUP, Universidade do Porto, Rua das Estrelas, P-4150-762 Porto, Portugal*
[36]*Departamento de Física e Astronomia, Faculdade de Ciências, Universidade do Porto, Rua do Campo Alegre, P-4169-007 Porto, Portugal*
[37]*Space Sciences, Technologies and Astrophysics Research (STAR) Institute, Université de Liège, Allée du 6 Août 19C, B-4000 Liège, Belgium*
[38]*Astrobiology Research Unit, Université de Liège, Allée du 6 Août 19C, B-4000 Liège, Belgium*
[39]*Astrophysics, Geophysics, And Space Science Research Center, Ariel University, Ariel 40700, Israel*
[40]*Department of Astronomy, Faculty of Physics, Sofia University 'St Kliment Ohridski', 5 James Bourchier Blvd, 1164 Sofia, Bulgaria*

This paper has been typeset from a TEX/LATEX file prepared by the author.